Zentrum für Technomathematik
Fachbereich 3 – Mathematik und Informatik

Nonlinear Inverse Unbalance Reconstruction in Rotor dynamics

Volker Dicken, Peter Maass, Ingo Menz,
Jenny Niebsch, Ronny Ramlau

Report 03–08

Berichte aus der Technomathematik

Report 03–08 July 2003

Nonlinear Inverse Unbalance Reconstruction in Rotor Dynamics

V. Dicken, P. Maaß, I. Menz, J. Niebsch, R. Ramlau *

August 18, 2003

Abstract

This paper is devoted to the identification and reconstruction of unbalance distributions in an aircraft engine rotor with a nonlinear damping element. We have developed a rotor model that takes into account the nonlinear behavior of a squeeze film damper between the engine's shaft and casing for large oscillation amplitudes. Based on the Tikhonov regularization for nonlinear ill–posed problems, we provided a three–step algorithm that enables us to identify and reconstruct single and distributed unbalances from data measured at the casing of the engine. In view of practical capability, the algorithms were accelerated to meet the requirement of tolerable computation time for larger models, too. [1]

Keywords: Rotor unbalance, nonlinear damping, nonlinear inverse problem, Tikhonov regularization

MSC (1991) 65R30, 73D35, 73D50

1 Introduction

Weight reduction efforts in aeroengine design lead to flexible casing structures, sensitive to vibration excitation from the main rotors. However the market demands the smallest possible level of vibrations transmitted to the aircrafts, in

*Corresponding authors: Ronny Ramlau and Jenny Niebsch, Zentrum für Technomathematik, Universität Bremen, D-28344 Bremen, Germany, email: ramlau/niebsch@math.uni-bremen.de

[1]The presented work was supported by the BMBF project "Inverse Bestimmung von Unwuchtverteilungen in Flugzeugtriebwerken"

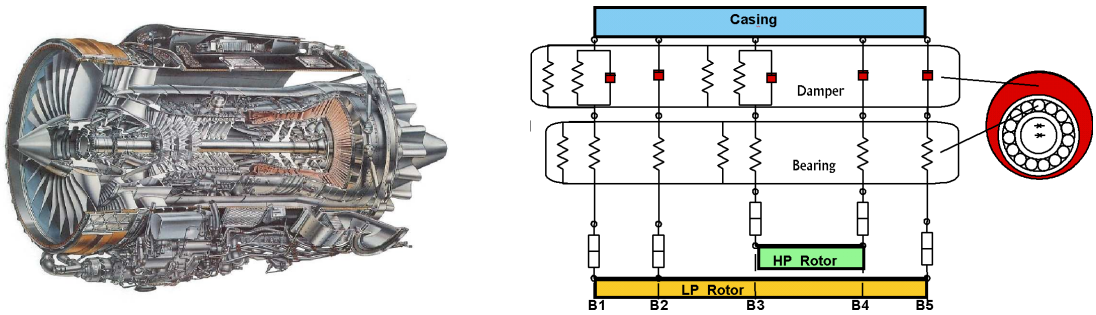

Figure 1: Engine interior and mechanical model with squeeze film damper

order to maximize passenger comfort. This holds especially true for the market segment of long range business aircrafts, where engines are generally mounted directly to the fuselage, and low cabin noise and vibration levels are essential in meeting customer expectations. Lowering vibrations caused by unbalances in the rotating parts may also help to increase safety and lifespan of aircrafts through reducing material fatigue. Since low pressure turbine synchronous vibration levels can be reduced with standard trim balancing methods with relatively little effort and expense, the focus is on reducing vibrations excited by the unbalance distribution on the high pressure (HP) rotor (compressor, turbine and coupling). The HP shaft is not accessible after the engine is assembled, which enforces the principle of 'right first time' on balancing and assembly. A direct measurement of HP vibrations in the assembled engine is impossible, due to narrow space, high forces and temperature, therefore we have to rely on indirect measurements and hence have to solve an inverse problem.

First results on the inverse reconstruction of distributed rotor unbalances from measurements at the casing were achieved in a feasibility study by Rienäcker et. all. [12] from the BMW Rolls–Royce GmbH, and in a cooperation project between Rolls–Royce Deutschland and the AG Technomathematik of the University of Bremen (part of the CERES project, [2]). Both treat the task as a linear problem using a linear whole engine FEM model developed at the BMW Rolls–Royce Group and programmed in NASTRAN for the forward computation and the construction of the inverse problem operator. In both cases it was possible to reconstruct continuous unbalance distributions like bend or wave deformation, but they failed in the identification of point unbalance positions. It was only possible to give hints in which part of the HP rotor the unbalance was situated. One possible reason for the failure of this first attempt seemed to be the linearity of the NASTRAN model since it did not take into account nonlinear damping effects arising from squeeze film dampers at the bearing of the rotor (see Figure 1). Hence it was our aim to develop a nonlinear model and check if it provides better reconstruction and identification results. Since it was to complicated to change the NASTRAN model, we employed a phantom turbine model based on finite element methods for flexible shafts. The parameters of the model were

trimmed to meet the characterizing properties of a high pressure rotor of an aircraft engine, like dimensions, eigenforms and resonance frequencies.
The solution of the forward problem, i.e. the computation of the vibration of the engine for a given unbalance distribution can be found by solving a nonlinear differential equation. As the forward problem is nonlinear, the inverse problem of identifying unbalances from data measured at certain sensor positions at the housing is nonlinear, too. For its solution, we have used Tikhonov regularization. Based on our model for the rotor, we employed a three-step algorithm which enables us to identify and reconstruct continuous as well as discontinuous unbalances like single point unbalances or combinations of point unbalances. All reconstructions were done in presence of about 15% data error. Our approach could also help if we are not specifically interested in the unbalance position but in a good balancing result with three given positions for balancing masses (like usual in practise). It allows to compute balancing recommendations (mass and angle) for the admitted balancing positions.

The paper is organized as follows: In Section 2 we introduce the above mentioned phantom gas turbine. Details like the organization of the matrices appearing in the model equation, and physically properties are carefully derived. This part is probably more interesting for the engineers among the readers. Section 3 gives a brief introduction to inverse ill-posed problems and their solution. The Tikhonov regularization as one possible solution technique will be introduced. Section 4 is devoted to the forward problem. Starting from the model equation, we construct a nonlinear operator equation of the form $A \cdot f = g$ describing our problem. Here f denotes the unbalance distribution and g the data measured at the casing of the engine. The solution of the forward problem, i.e. computing g from given f, is contained in this section, too.
Section 5 is concerned with the inverse problem of determining f from given (possibly noisy) data g. In particular the derivative of A and its adjoint are computed, which is necessary to apply Tikhonov regularization. Moreover we present an idea how to accelerate the minimization of the Tikhonov functional, and derive the reconstruction algorithm in this section. Finally, Section 6 contains the results of our test computations and the final three–step algorithm arising from the interpretation of the first reconstruction results. We demonstrate how single and distributed unbalances can be identified and reconstructed, and how the data error influences the reconstructions. We also show how the algorithm works for balancing suggestions if balancing positions are previously fixed.

2 Gas turbine model

In this section we want to establish a gas turbine model based on flexible shafts. Usually such a system is described by an equation of the form

$$M\mathbf{u}'' + S\mathbf{u} = \Omega^2\mathbf{p} \tag{1}$$

with M being the mass or inertia matrix, S the stiffness matrix, $\mathbf{u}$ the vector of the degrees of freedom, $\mathbf{p}$ the unbalanced load vector, and Ω the frequency. In the presence of damping, and assuming an unbalance $\mathbf{f}$ as the causing load, the equation has the form

$$M\mathbf{u}'' + D\mathbf{u}' + S\mathbf{u} = \Omega^2 P\mathbf{f}. \tag{2}$$

Here D is the sparse damping matrix, $\mathbf{f}$ the vector of unbalances, and P is a matrix that assigns the forces caused by $\mathbf{f}$ to the degrees of freedom in the FEM model.

2.1 Modelling of a flexible shaft using Finite Elements

The usual technique for calculating the dynamic behaviour of flexible shafts is the Finite Element Method (FEM). To get an equation of the type (1), the rotor is divided into similar elements (see Figure 2). For each node the chosen degrees of freedom have to take into account all geometric boundary and transition conditions.

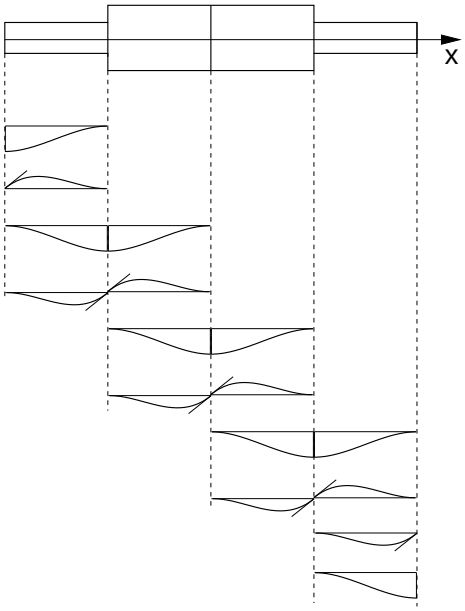

Figure 2: Flexible shaft, finite beam elements, degrees of freedom

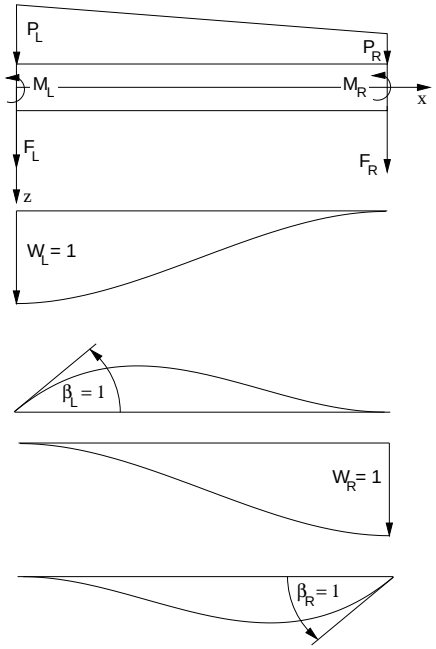

Figure 3: Finite beam elements, loads, shape functions, degrees of freedom

Each finite beam element is treated separately. The motion of the element is described by shape functions (Figure 3). Their scaleable amplitudes are the

degrees of freedom $W_L,\ \beta_L$ of the left node and $W_R,\ \beta_R$ of the right one. They are ordered by

$$\mathbf{u}_e^T = [W_L \quad \beta_L \quad W_R \quad \beta_R]. \tag{3}$$

From this ordering results the order of external forces and moments

$$\mathbf{p}_e^T = [F_L \quad M_L \quad F_R \quad M_R]. \tag{4}$$

The characteristics of the beam element are given by its stiffness matrix S_e, and its inertia or mass matrix M_e . The influence of a continuous load is described by the element load vector p_e. The element matrices and the element load vector are derived by an energy formulation (see [4]). As mentioned in the introduction the model parameter are chosen such that the model is very close to the high preasure rotor of an aircraft engine. Thus the stiffness matrix was derived as

$$S_e = \frac{E \cdot I_{ax}}{L^3} \begin{pmatrix} 12\psi & -6L\psi & -12\psi & -6L\psi \\ -6L\psi & L^2(1+3\psi) & 6L\psi & L^2(-1+3\psi) \\ -12\psi & 6L\psi & 12\psi & 6L\psi \\ -6L\psi & L^2(-1+3\psi) & -6L\psi & L^2(-1+3\psi) \end{pmatrix}. \tag{5}$$

E is Young's modulus, for steel we have $E = 208GPa$. For round beams the axial moment of inertia is given by

$$I_{ax} = \pi \cdot \frac{d_{out}^4 - d_{in}^4}{64} \tag{6}$$

with d_{out} for the outer diameter and d_{in} for the inner diameter of the shaft. The length of the element is represented by L. The shear parameter is given by ([7])

$$\psi = \frac{1}{1 + 12\frac{E \cdot I_{ax}}{L^2 \cdot G \cdot A_s}} \tag{7}$$

where G is the shear modulus

$$G = \frac{E}{2(1+\nu)} \tag{8}$$

with Poisson's ratio ν. For steel ν equals 0.28. For round beams the effective shear area

$$A_s = A \cdot k_s \tag{9}$$

is derived from the area of the cross section

$$A = \frac{\pi}{4}(d_{out}^2 - d_{in}^2) \tag{10}$$

and the shear coefficient [1]

$$k_s = \frac{6(1+\nu)(1+m^2)^2}{(7+6\nu)(1+m^2)^2 + (20+12\nu)m^2} \tag{11}$$

where

$$m = \frac{d_{in}}{d_{out}}. \tag{12}$$

The matrix of inertia is superimposed of two parts

$$M_e = M_{\mu e} + M_{\tilde{\mu} e}. \tag{13}$$

The first part corresponds to the translatorial mass per length

$$\mu = \varrho \cdot A \tag{14}$$

where ϱ is the density of the material. For steel $\varrho = 7850 kg m^{-3}$. We have (see [4])

$$M_{\mu e} = \frac{\mu L}{840} \times \tag{15}$$
$$\begin{pmatrix} 280{+}28\psi{+}4\psi^2 & -L(35{+}7\psi{+}2\psi^2) & 140{-}28\psi{-}4\psi^2 & L(35{-}7\psi{-}2\psi^2) \\ -L(35{+}7\psi{+}2\psi^2) & L^2(7{+}\psi^2) & -L(35{-}7\psi{-}2\psi^2) & -L^2(7{-}\psi^2) \\ 140{-}28\psi{-}4\psi^2 & -L(35{-}7\psi{-}2\psi^2) & 280{+}28\psi{+}4\psi^2 & L(35{+}7\psi{+}2\psi^2) \\ L(35{-}7\psi{-}2\psi^2) & -L^2(7{-}\psi^2) & L(35{+}7\psi{+}2\psi^2) & L^2(7{+}\psi^2) \end{pmatrix}.$$

The second part takes respect to the rotational mass per length

$$\tilde{\mu} = \varrho \cdot I_{ax},$$
$$M_{\tilde{\mu} e} = \frac{\tilde{\mu}}{30L} \times \tag{16}$$
$$\begin{pmatrix} 36\psi^2 & L(15\psi{-}18\psi^2) & -36\psi^2 & L(15\psi{-}18\psi^2) \\ L(15\psi{-}18\psi^2) & L^2(10{-}15\psi{+}9\psi^2) & -L(15\psi{-}18\psi^2) & L^2(5{-}15\psi{+}9\psi^2) \\ -36\psi^2 & -L(15\psi{-}18\psi^2) & 36\psi^2 & -L(15\psi{-}18\psi^2) \\ L(15\psi{-}18\psi^2) & L^2(5{-}15\psi{+}9\psi^2) & -L(15\psi{-}18\psi^2) & L^2(10{-}15\psi{+}9\psi^2) \end{pmatrix}.$$

The element load vector due to continuous load results in

$$p_e = \frac{L}{120} \begin{pmatrix} 40+2\psi & 20-2\psi \\ -L(5+\psi) & -L(5-\psi) \\ 20-2\psi & 40+2\psi \\ L(5-\psi) & L(5+\psi) \end{pmatrix} \cdot \begin{pmatrix} p_L \\ p_R \end{pmatrix} \tag{17}$$

where p_L denotes the force per length at the left node and p_R the force per length at the right node.

To build the system matrices S and M, the element matrices S_e [see (5)], M_e [see (13)-(16)] resp., are combined by superimposing the elements affecting the right node of the ith element matrix with the ones belonging to the left node of the $(i+1)$st element matrix (Figure 4). The load vector $\mathbf{p}$ is build by superimposing the element load vectors p_e [see (17)] in an analogous manner.

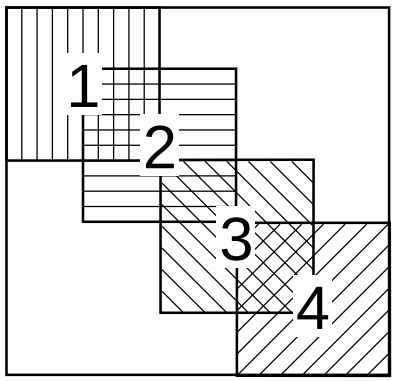

Figure 4: System matrix, superimposed element matrix

2.2 Gas turbine

The gas turbine shown in Figure 5 is modelled as a system of flexible shafts by 44 finite beam elements. Each of the eight disks is modelled by one element, the coupling between the compressor and the turbine consists of two elements. The remaining 34 elements are distributed over the shaft.

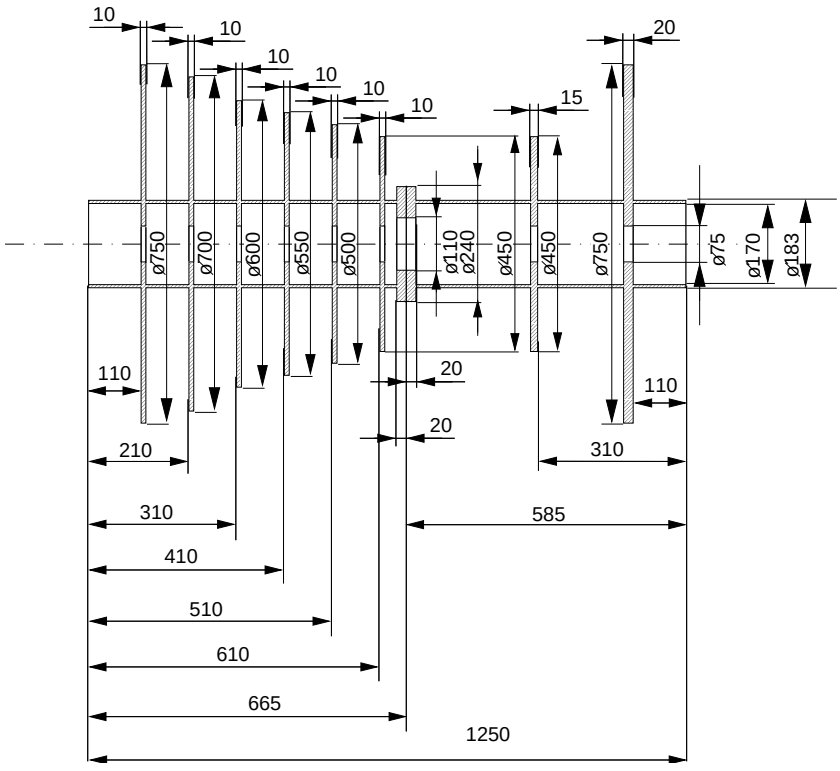

Figure 5: Flexible shafts (gas turbine)

Figure 6 shows the first three elastic eigenforms derived from this model. The

corresponding eigenfrequencies are 199 Hz (11940 rpm), 392 Hz (23520 rpm) and 652 Hz (39120 rpm).

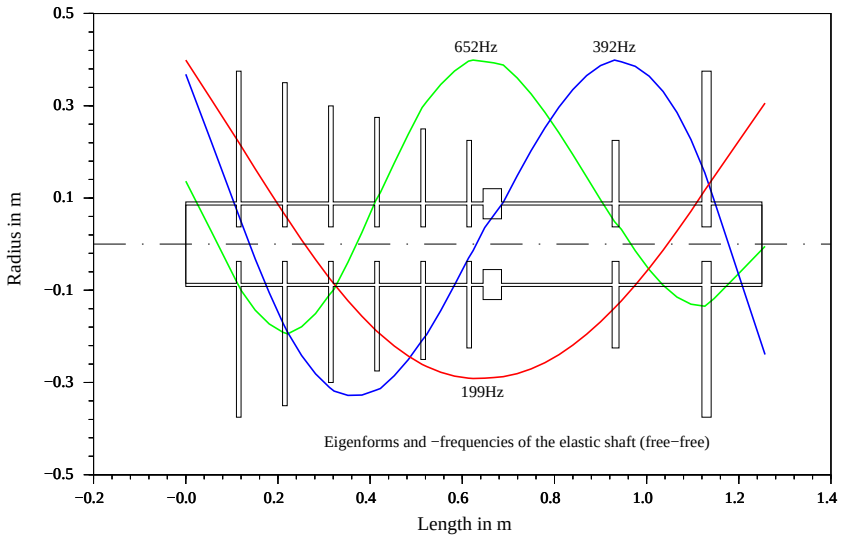

Figure 6: Elastic eigenforms and eigenfrequencies, free–free

These free-free eigenfrequencies and eigenforms are modified by the turbine's elastic bearings and the housing which is supported elastically too. To keep the calculation simple, also the housing is modelled as a flexible shaft (Figure 7).

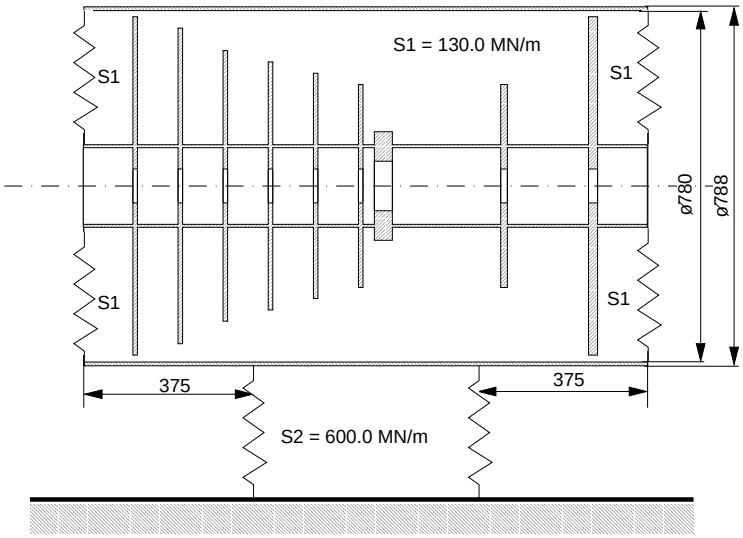

Figure 7: Turbine, housing and elastic bearings

The bearings are assumed to be isotropic, and gyroscopic effects are neglected. Modelling the system this way, the equations of the horizontal plane are decoupled from the ones of the vertical plane.

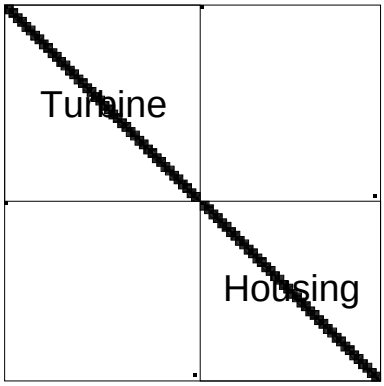

Figure 8: Block diagonal matrix structure, non zero off diagonal elements due to elastic bearings (black squares)

Since the forces of the turbine's elastic bearings are proportional to the relative displacement of the turbine's node and the node of the housing

$$F_{Turb} = s \cdot (w_{Turb} - w_{Hous}), \tag{18}$$

the bearing's stiffness s appears in the row of the related turbine's degree of freedom at the columns of both envolved nodes. Due to Newton's principle of actio and reactio,

$$F_{Hous} = -F_{Turb}, \tag{19}$$

it has to be invented in the related row of the housing's degree of freedom too. The four coefficients make up a rectangle with positve elements s at the corners on the diagonal and negative elements $-s$ at the off diagonal corners. The elastic bearings of the housing are supported by a rigid founding. So the stiffnes appears on the diagonal elements only. The structure of the resulting stiffness matrix S is shown in Figure 8.

The eigenfrequencies and eigenforms which result from the model in Figure 7 are shown in Figure 9. Assuming a maximum speed of 17000 rpm (283 Hz) the turbine crosses two critical speeds at 6060 rpm (101 Hz) and at 8280 rpm (138 Hz). The third critical speed at 17940 rpm (299 Hz) is not crossed but approached by 95%. The forth eigenfrequency is found at 22980 rpm (383 Hz). It is above the range of operating speed. The fifth eigenfrequency at 35700 rpm (595 Hz) is dominated by movements of the housing.

2.3 Model including a nonlinear squeeze film damper

Damping elements are added to the model in the same manner like the elastic bearings. But since the forces of a damper are proportional to the relative veloctiy

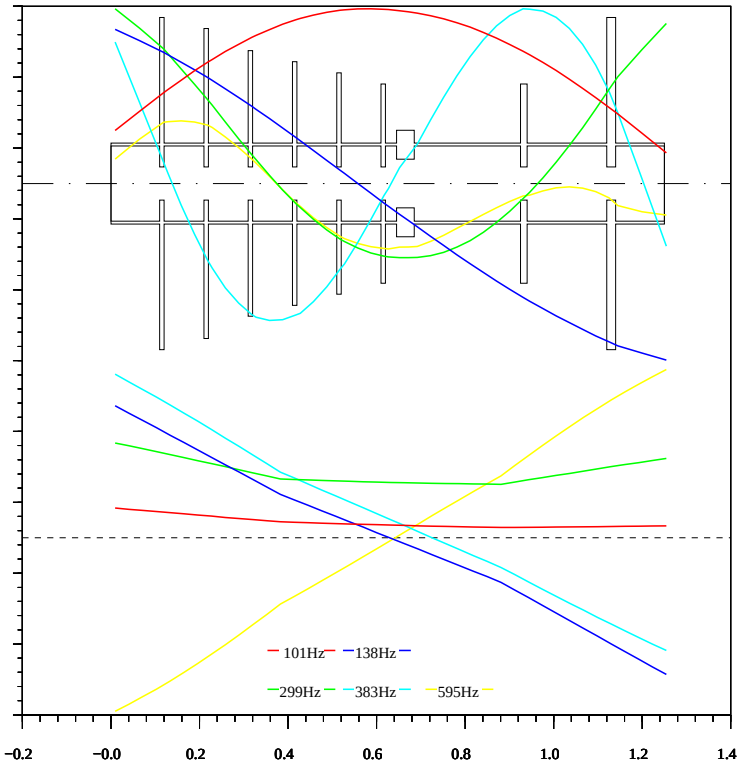

Figure 9: Eigenforms and eigenfrequencies

of the envolved turbine's and housing's nodes the related force on the turbine is given by

$$F_{Turb} = d \cdot (\dot{w}_{Turb} - \dot{w}_{Hous}) \tag{20}$$

with d being the damping coefficient. The related damping matrix from (2) is very sparse. The only non-zero entries make up a rectangle of four entries for each damper like the elastic bearing does for the stiffness matrix.

At the nearly undamped aircraft engines, squeeze film dampers are used to reduce the vibration. They fit for the reduction of unbalance induced vibration especially due to their increasing damping rate at higher vibration. Figure 11 from [5] shows a schematic of a squeeze film damper. Detailes shown in Figure 12 are taken from [6]. The damping arises from the shaft's vibration in a narrow oil filled gap. The rolling contact bearing is used for separation of the rotating shaft from the non rotating oil film only. It does not take any static load.
The squeeze film damper is a pure damping element. The damping characteristic of a squeeze film damper is nonlinear, when the strength of the damping increases by the level of vibration. In the theory of journal bearings parameters for a general description of the damping behaviour can be given in order to avoid time wasting time step integration of the differential equations. Unfortunately no specific parameters can be given for squeeze film dampers. Only in the special

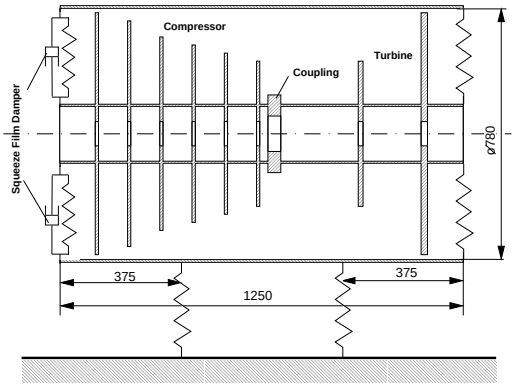

Figure 10: Rotor model with squeeze film damper

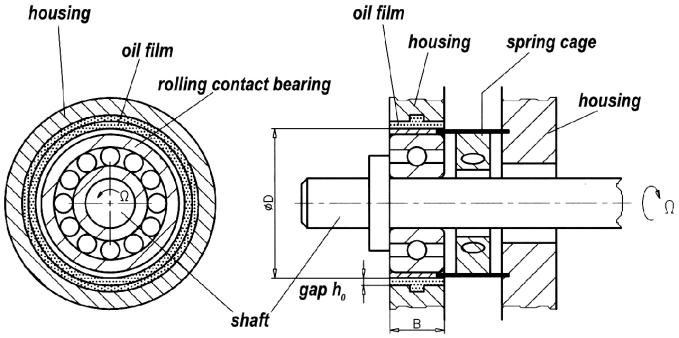

Figure 11: Schematic of a squeeze film damper

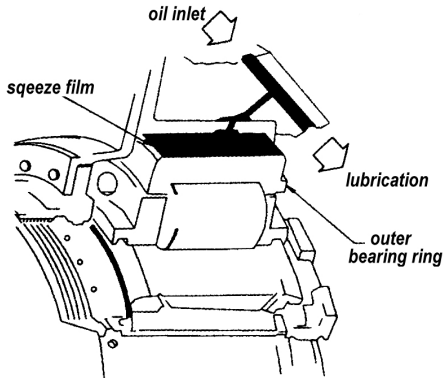

Figure 12: Details of a squeeze film damper

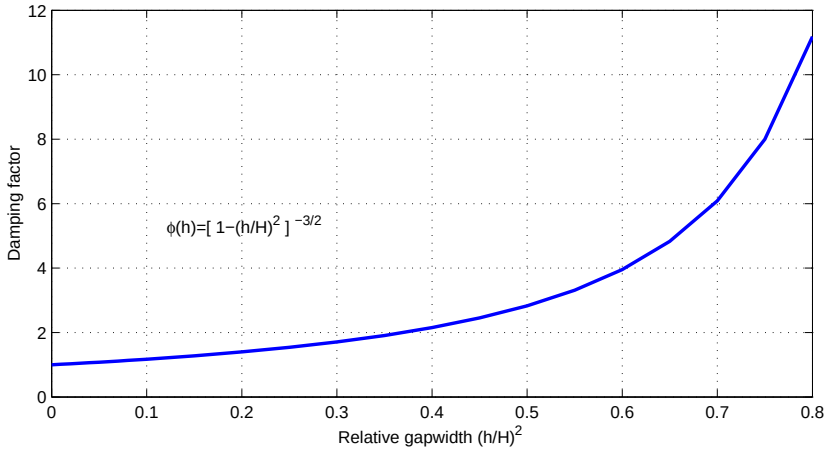

Figure 13: Damping characteristic of a squeeze film damper

case of circular shaft orbits the equations of motion can be linearized. In the case of infinite vibration the damping is a function of the oil's viscosity and the bearing's geometry only. For higher vibration the damping coefficent of the squeeze film damper can be calculated from Figure 13 as a multiple of the one related to infinte vibration [5].

3 A short summary on ill–posed inverse problems

In recent years the theory of treating nonlinear ill–posed problems was well established. For an overview see [3, 8]. For the following, let A be a linear or nonlinear operator between real Hilbert spaces. With given data g, we want to find a solution f of the equation

$$Af = g. \tag{21}$$

The problem is called ill–posed, if the solution f does not depend continuously on the data g. In fact, if we only have noisy data with noise level δ, i.e. $\|g^\delta - g\| \leq \delta$, then (provided the inverse A^{-1} exists) $f^\delta = A^{-1}g^\delta$ might be an arbitrarily bad approximation to a solution of (21). To obtain a stable solution, one has to use so called regularization methods. The general idea is to approximate the discontinuous inverse operator by a family of continuous operators T_α. The regularization parameter α has to be chosen such that $\lim_{\delta\to 0} \alpha(\delta, f^\delta) = 0$ holds. For nonlinear operators, equation (21) might have several solutions. Thus we choose the concept of a $\bar{f}$–minimum–norm solution, i.e. we are looking for a solution closest to an a priory given function $\bar{f}$.

A prominent example for a regularization method is Tikhonov regularization. The regularization operator is defined by

$$T_\alpha g^\delta = f_\alpha^\delta = \arg\min_f J_\alpha(f) \tag{22}$$

with the Tikhonov functional given by

$$J_\alpha(f) = \|g^\delta - Af\|^2 + \alpha\|f - \bar{f}\|^2. \tag{23}$$

For the determination of the regularization parameter α, we can use the so called Morozov's discrepancy principle where α is chosen s.t.

$$\delta \leq \|g^\delta - Af_\alpha^\delta\|^2 \leq c\delta \tag{24}$$

holds [13, 9]. For linear operators, the minimizer of the Tikhonov functional can be computed by solving a linear system. In case of a nonlinear operator, optimization methods have to be used additionally to compute a minimizer of (23). A classical approach to minimize the functional $J_\alpha(f)$ is the use of gradient methods. The gradient of the Tikhonov functional is given by

$$\frac{1}{2}\nabla J_\alpha(f) = A'(f)^*(Af - g^\delta) + \alpha(f - \bar{f}), \tag{25}$$

where the linear operator $A'(f)^*$ is the adjoint of the derivative of A at the point f [10].

4 The forward problem

As we consider a model with nonlinear damping provided by a squeeze film damper, equation (2) changes to

$$M\mathbf{u}'' + D(\mathbf{u})\mathbf{u}' + S\mathbf{u} = \Omega^2 P\mathbf{f}, \tag{26}$$

where D is a function of the solution $\mathbf{u}$. This is due to the fact that the damping of a squeeze film damper depends on the amplitude of the oscillation. The damping is modeled by (see Figure 13)

$$D(\mathbf{u}) = \bar{D} \cdot \varphi(|h(\mathbf{u})|^2) \tag{27}$$

$$\text{with} \quad \varphi(s) = \left(1 - \frac{s}{H^2}\right)^{-\frac{3}{2}}, \tag{28}$$

$$h(\mathbf{u}) = u_{in} - u_{out}. \tag{29}$$

Here H is the maximal gap width in the squeeze film damper, h is the actual gap width which is the difference between u_{in}, the degree of freedom of the damper position at the shaft, and u_{out}, the degree of freedom of the damper position at the housing. Clearly equation (26) is nonlinear in $\mathbf{u}$, and the solution can not be computed directly. To simplify the problem, we want to assume that we only have a squeeze film damper at one bearing and constant damping at the other one, hence

$$D(\mathbf{u}) = D_0 + D_1 \cdot \varphi(|h(\mathbf{u})|^2). \tag{30}$$

4.1 Construction of the forward operator

The solution of (26) with (27)-(30) are the degrees of freedom of every knot of the model. However, measurements can only be taken at certain sensor positions. We want to modify the solution operator of equation (26) in such a way that it maps the causing unbalance vector to the oscillation vector of the knots at the sensor positions. In the following we assume that we have

- s sensors
- N sources of unbalances
- L degrees of freedom
- K frequencies $\{\Omega_1, \cdots, \Omega_K\}$.

The solution operator
Inserting the ansatz

$$\begin{aligned} \mathbf{u}(t) &= \mathbf{u}^+ e^{i\Omega t} + \mathbf{u}^- e^{-i\Omega t} \\ \mathbf{f}(t) &= \mathbf{f}^+ e^{i\Omega t} + \mathbf{f}^- e^{-i\Omega t} \end{aligned} \tag{31}$$

in (26), we get the following solution

$$\mathbf{u}^\pm = [\underbrace{-M + \Omega^{-2} S \pm i\Omega^{-1} D_0}_{C_\Omega} \pm \underbrace{i\Omega^{-1} D_1}_{D_\Omega} \cdot \varphi(|h(\mathbf{u})|^2)]^{-1} P\mathbf{f}^\pm. \tag{32}$$

As $h = h(\mathbf{u})$, this is a fixed–point equation for $\mathbf{u}^\pm$.

Real notation
Up to here we have used complex notation in all formulae. Now we want to shift to real notation. The main reason for the shifting is that for Tikhonov regularization, which will be used for solving the problem, a convergence analysis is only available for the real case. To that end we use the representation

$$\begin{aligned} \mathbf{u}(t) &= \mathbf{u}^c \cos(\Omega t) + i\mathbf{u}^s \sin(\Omega t), \\ \mathbf{u}^c &= 2\Re(\mathbf{u}^+), \\ \mathbf{u}^s &= -2\Im(\mathbf{u}^+). \end{aligned}$$

This means that we only need $\mathbf{u}^+$. Denoting

$$C_\Omega := -M + \Omega^{-2} S + i\Omega^{-1} D_0, \tag{33}$$

$$D_\Omega := i\Omega^{-1} D_1, \tag{34}$$

(cf. (32)) we get

$$\begin{aligned} \mathbf{u}^c &= 2\Re([C_\Omega + D_\Omega\varphi(|h|^2)]^{-1}P\mathbf{f}^+) \\ \mathbf{u}^s &= -2\Im([C_\Omega + D_\Omega\varphi(|h|^2)]^{-1}P\mathbf{f}^+). \end{aligned}$$

With the additional abbreviation

$$H_\Omega(\varphi(|h|^2)) := C_\Omega + D_\Omega\varphi(|h|^2) \tag{35}$$

and the notation

$$\mathbf{f}_r = (\Re(\mathbf{f}^+), \Im(\mathbf{f}^+))^T,$$

where the superscript T stands for the transpose, we arrive at the real notation for the solution $\mathbf{u}$ of (26):

$$\mathbf{u}_r = \begin{pmatrix} \mathbf{u}^c \\ \mathbf{u}^s \end{pmatrix} = 2 \begin{pmatrix} \Re(H_\Omega(\varphi(|h|^2))^{-1}P) & -\Im(H_\Omega(\varphi(|h|^2))^{-1}P) \\ \Im(H_\Omega(\varphi(|h|^2))^{-1}P) & \Re(H_\Omega(\varphi(|h|^2))^{-1}P) \end{pmatrix} \mathbf{f}_r. \tag{36}$$

The measurement process
We will denote the real formulation of the measured data $\mathbf{g} \in \mathbb{C}^s$ at frequency Ω and the real formulation of h by

$$\mathbf{g}_r(\Omega) = (\Re(\mathbf{g}(\Omega)), \Im(\mathbf{g}(\Omega)))^T \in \mathbb{R}^{2s}, \tag{37}$$

$$\mathbf{h}(\Omega) = (\Re(h(\Omega)), \Im(h(\Omega)))^T \in \mathbb{R}^2. \tag{38}$$

Thus we have for the unbalance vector $\mathbf{f}_r \in \mathbb{R}^{2N}$ and $\mathbf{u}_r = (\mathbf{u}^c, \mathbf{u}^s)^T \in \mathbb{R}^{2L}$. Further we assume that

- Q_1 is the matrix that extracts $\mathbf{u}$ at the sensor positions:

$$\begin{pmatrix} Q_1 & 0 \\ 0 & Q_1 \end{pmatrix} \mathbf{u}_r = \mathbf{g}_r.$$

- Q_2 is the matrix that extracts $\mathbf{h}$ from $\mathbf{u}_r$:

$$\begin{pmatrix} Q_2 & 0 \\ 0 & Q_2 \end{pmatrix} \mathbf{u}_r = \mathbf{h}.$$

Inserting these definitions in (36), the forward problem can be written for a fixed frequency Ω as

$$\begin{pmatrix} \mathbf{g}_r(\Omega) \\ \mathbf{h}(\Omega) \end{pmatrix}_{\mathbb{R}^{2s+2}} = 2 \begin{pmatrix} \Re(Q_1H_\Omega(\varphi(|h|^2))^{-1}P) & -\Im(Q_1H_\Omega(\varphi(|h|^2))^{-1}P) \\ \Im(Q_1H_\Omega(\varphi(|h|^2))^{-1}P) & \Re(Q_1H_\Omega(\varphi(|h|^2))^{-1}P) \\ \Re(Q_2H_\Omega(\varphi(|h|^2))^{-1}P) & -\Im(Q_2H_\Omega(\varphi(|h|^2))^{-1}P) \\ \Im(Q_2H_\Omega(\varphi(|h|^2))^{-1}P) & \Re(Q_2H_\Omega(\varphi(|h|^2))^{-1}P) \end{pmatrix} \mathbf{f}_r. \tag{39}$$

For better readability we will use the abbreviations

$$\begin{aligned}
\Pi_{\mathbf{g}} A_\Omega(\varphi(|h|^2)) &:= 2\begin{pmatrix} \Re(Q_1 H_\Omega(\varphi(|h|^2))^{-1}P) & -\Im(Q_1 H_\Omega(\varphi(|h|^2))^{-1}P) \\ \Im(Q_1 H_\Omega(\varphi(|h|^2))^{-1}P) & \Re(Q_1 H_\Omega(\varphi(|h|^2))^{-1}P) \end{pmatrix}, \\
\Pi_{\mathbf{h}} A_\Omega(\varphi(|h|^2)) &:= 2\begin{pmatrix} \Re(Q_2 H_\Omega(\varphi(|h|^2))^{-1}P) & -\Im(Q_2 H_\Omega(\varphi(|h|^2))^{-1}P) \\ \Im(Q_2 H_\Omega(\varphi(|h|^2))^{-1}P) & \Re(Q_2 H_\Omega(\varphi(|h|^2))^{-1}P) \end{pmatrix}, \\
A_\Omega(\varphi(|h|^2)) &:= \begin{pmatrix} \Pi_{\mathbf{g}} A_\Omega(\varphi(|h|^2)) \\ \Pi_{\mathbf{h}} A_\Omega(\varphi(|h|^2)) \end{pmatrix}. \qquad (40)
\end{aligned}$$

We remark that for fixed h the above terms are matrices which have the following sizes:

$$\begin{aligned}
H_\Omega(\varphi(|h|^2)) &\in \mathbb{C}^{L\times L} \\
Q_1 &\in \mathbb{R}^{s\times L} \\
Q_2 &\in \mathbb{R}^{1\times L} \qquad (41) \\
P &\in \mathbb{R}^{L\times N} \\
A_\Omega(\varphi(|h|^2)) &\in \mathbb{R}^{(2s+2)\times 2N}.
\end{aligned}$$

We only have to store the real and imaginary parts of $Q_1 H_\Omega(\varphi(|h|^2))^{-1}P \in \mathbb{R}^{s\times N}$ and $Q_2 H_\Omega(\varphi(|h|^2))^{-1}P) \in \mathbb{R}^{1\times N}$. An example for those matrices for a specified frequency and h– sample can be found under www.math.uni-bremen.de\~ramlau\unbalancematrices.

Theorem 1 *Let $\mathbf{g}_r(\Omega)$ be the real data vector containing the degrees of freedom at the sensor positions, $\mathbf{h}$ as defined in (29) and (38), and $\mathbf{f}_r$ the real notation of the unbalance vector. Then the data vector $\mathbf{g}_r$ for a given unbalance can be computed by*

$$\begin{pmatrix} \mathbf{g}_r(\Omega) \\ \mathbf{h}(\Omega) \end{pmatrix} = A_\Omega(\varphi(|h|^2))\ \mathbf{f}_r, \qquad (42)$$

where $A_\Omega(\varphi(|h|^2))$ is defined by (40).

4.2 Numerical solution of the forward problem

From now on we omit the index r denoting the real notation when no confusion is possible. Solving $g(\Omega) = \Pi_{\mathbf{g}} A_\Omega(\varphi(|h|^2))\ \mathbf{f}$ for given $\mathbf{f}$ would be easy if the correspondin $\mathbf{h}(\mathbf{f})$ is known. Finding $\mathbf{h}$ requires to solve

$$\mathbf{h}(\Omega) = \Pi_{\mathbf{h}} A_\Omega(\varphi(|h|^2))\mathbf{f}, \qquad (43)$$

which is a fixed–point equation for h. (We refer to (38) for the use of $\mathbf{h}$ and h.) If we have found h with (43), the matrix $\Pi_{\mathbf{g}} A_\Omega(\varphi(|h|^2))$ and thus $\mathbf{g}$ can be

computed immediately. In a first attempt, we have used the classical fixed–point iteration

$$\mathbf{h}_{k+1} = \Pi_{\mathbf{h}} A_\Omega(\varphi(|h_k|^2))\ \mathbf{f}$$

for solving (43), but found it rather time consuming, since for each h_k the matrices $Q_2 H_\Omega(\varphi(|h_k|^2))^{-1} P$ have to be computed. Moreover, this process has to be done for each frequency. As for inverse problems the forward problem has to be solved quite often, this is not practicable. Instead, we found the following approach more suitable:
As we have seen above, $A_{\Omega_k}(\varphi(|h|^2))$ is a matrix for every given h. Thus, we can precompute for a sample of $|h|^2$, $\{|h_1|^2, \ldots, |h_{I_{max}}|^2\}$, the corresponding matrices

$$[A_{\Omega_k}(\varphi(|h_i|^2))]_{i=1,\ldots,I_{max},\ k=1,\ldots,K}$$

and store them in advance. Now for a given unbalance $\mathbf{f}$ we only have to pick the matrix which fulfills (at least approximately)

$$\mathbf{h}_i = \Pi_{\mathbf{h}} A_{\Omega_k}(\varphi(|h_i|^2))\mathbf{f}. \tag{44}$$

A promising fixed–point candidate for (44) is a zero of the real valued function

$$p(h_i) = |\mathbf{h}_i|^2 - |\Pi_{\mathbf{h}} A_\Omega(\varphi(|h_i|^2))\mathbf{f}|^2. \tag{45}$$

For finding such a zero h_z of p, the function fzero of matlab was employed. It interpolates p and computes an approximative zero of the interpolated function. Thus the algorithm for the forward computation reads as follows:

- Given $\mathbf{f}$, $\{|h_1|^2, \ldots, |h_{I_{max}}|^2\}$ and Ω
- $p(h_i) = |\mathbf{h}_i|^2 - |\Pi_{\mathbf{h}} A_\Omega(\varphi(|h_i|^2))\mathbf{f}|^2$.
- $h_z = \mathbf{fzero}(p(h_i))$ (46)
- Compute $\Pi_{\mathbf{g}} A_\Omega(\varphi(|h_z|^2))$ as Lagrange interpolation of $\Pi_{\mathbf{g}} A_\Omega(\varphi(|h_i|^2))$ at h_z
- $\mathbf{g}(\Omega) = \Pi_{\mathbf{g}} A_\Omega(\varphi(|h_z|^2)) \cdot \mathbf{f}$ (47)

In all our test computations, the zero of $p(h_i)$ was unique, which means that we had $|h|^2$ correctly identified. In general, the found zero $|h_z|^2$ is different from our samples $|h_i|^2$, thus we have used Lagrange interpolation of order 2 to interpolate the matrices $A_{\Omega_k}(\varphi(|h_i|^2))$ and finally compute $A_{\Omega_k}(\varphi(|h_z|^2))$. We have implemented both the classical fixed point method and the above described method for the solution of the forward problem. Several test computations assured us that they both give the same results, but our approach was much faster.
In view of (39) we only have to store the matrix

$$\begin{pmatrix} \Re(Q_1 H_{\Omega_k}(\varphi(|h_i|^2)))^{-1} P) & \Im(Q_1 H_{\Omega_k}(\varphi(|h_i|^2))^{-1} P) \\ \Re(Q_2 H_{\Omega_k}(\varphi(|h_i|^2)))^{-1} P) & \Im(Q_2 H_{\Omega_k}(\varphi(|h_i|^2))^{-1} P) \end{pmatrix} \in I\!R^{(s+1)\times 2N},$$

(see (41)) for each $\Omega_k,\ k = 1, \cdots, K$ and each $|h_i|^2,\ i = 1, \cdots, I_{max}$. Doing this the entire matrix to be stored is of size $K \cdot (s+1) \times 2N \cdot I_{max}$. Thus we can handle the forward problem with maintainable amount of time and storage. Figure 14 shows the movement in the squeeze film damper caused by a real unit unbalance at the third disc.

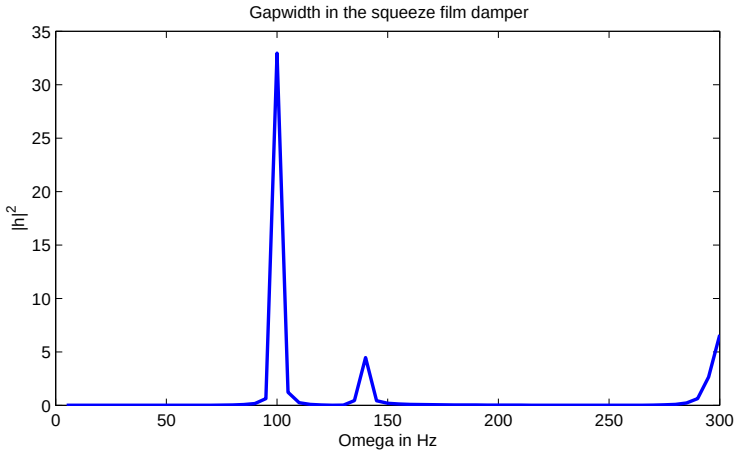

Figure 14: Forward model: Oscillation in the squeeze film damper. We pass two resonance frequencies at 101Hz and 138Hz, and approach a third one at 299Hz.

5 The inverse problem

Knowing the measured data $\mathbf{g}^\delta(\Omega)$ at the sensor positions for each frequency Ω, the inverse problem consists in finding $\mathbf{f}$ with

$$\mathbf{g}^\delta(\Omega) = \Pi_{\mathbf{g}} A_\Omega(\varphi(|h|^2))\ \mathbf{f} \tag{48}$$

$$\text{and} \qquad \mathbf{h}(\Omega) = \Pi_{\mathbf{h}} A_\Omega(\varphi(|h|^2))\ \mathbf{f}. \tag{49}$$

It is well known from the theory of linear damped systems, that the reconstruction of the causing unbalance from measured oscillation data is ill–posed. Thus we have to use regularization methods. A widely used algorithm to solve ill–posed inverse problems is Tikhonov regularization which we have briefly described in section 3. Tikhonov regularization requires to use an algorithm for the minimization of the Tikhonov functional. For iterative algorithms, the gradient $\nabla J_\alpha(f)$ (see (25)) of the Tikhonov functional with nonlinear operator A plays a central role. For steepest descent methods, $\nabla J_\alpha(f)$ is used as a search direction, and for fixed point or Newton's method, a function with

$$\nabla J_\alpha(f) = 0$$

is searched for. According to (25), the computation of $\nabla J_\alpha(f)$ requires the knowledge of the Fréchet derivative $A'(f)$ of A and its adjoint $A'(f)^*$. For our problem

we have

$$\begin{aligned} f &= \mathbf{f} \in I\!R^{2N}, \\ g^\delta &= \begin{pmatrix} \mathbf{g}^\delta(\Omega_1) \\ \vdots \\ \mathbf{g}^\delta(\Omega_K) \end{pmatrix} \in I\!R^{2s\cdot K}, \\ A &= \Pi_{\mathbf{g}} \begin{pmatrix} A_{\Omega_1} \\ \vdots \\ A_{\Omega_K} \end{pmatrix} : I\!R^{2N} \longrightarrow I\!R^{2s\cdot K}, \\ A' &= \Pi_{\mathbf{g}} \begin{pmatrix} A'_{\Omega_1} \\ \vdots \\ A'_{\Omega_K} \end{pmatrix} : I\!R^{2N} \longrightarrow I\!R^{2s\cdot K}, \\ A'(f)^* &= \Pi_{\mathbf{g}} \begin{pmatrix} A'_{\Omega_1}(\mathbf{f})^* \dots A'_{\Omega_K}(\mathbf{f})^* \end{pmatrix} : I\!R^{2s\cdot K} \longrightarrow I\!R^{2N}. \end{aligned} \tag{50}$$

Here we have shorten the notation of $A_{\Omega_k}(\varphi(|h|^2))$ to A_{Ω_k}.

5.1 Derivative of the forward operator and its adjoint

To find a formula for the derivative we have used the Implicit Function Theorem (IFT) which states the following: Provided a function $y = y(x)$ is implicit defined via $F(x, y) = 0$, and $F'(x_0, y_0)$ exists and $F_y(x_0, y_0)$ is invertible, then y is differentiable in x_0 and

$$y'(x_0) = -F_y(x_0, y(x_0))^{-1} F_x(x_0, y(x_0)).$$

Theorem 2 *Each component of the Frèchet derivative $A'(f)$ of A given in (50) is computed by*

$$\Pi_{\mathbf{g}} A'_\Omega(\mathbf{f})\mathbf{v} = \Pi_{\mathbf{g}} A_\Omega \mathbf{v} - 2\varphi'(|\mathbf{h}|^2) \frac{\langle \mathbf{h}, \Pi_{\mathbf{h}} A_\Omega \mathbf{v} \rangle}{1 + 2\varphi'(|\mathbf{h}|^2)\langle \mathbf{h}, \Pi_{\mathbf{h}} B_\Omega \mathbf{f} \rangle} \Pi_{\mathbf{g}} B_\Omega \mathbf{f}. \tag{51}$$

Proof: We set

$$F(x, y) := F(\mathbf{f}, (\mathbf{g}, \mathbf{h})) = \begin{pmatrix} \mathbf{g} \\ \mathbf{h} \end{pmatrix} - A_\Omega(\varphi(|\mathbf{h}|^2))\ \mathbf{f} = \mathbf{0}.$$

To extract the derivative of $A_\Omega(\varphi(|\mathbf{h}|^2))$, we concider

$$\mathbf{g} = \Pi_{\mathbf{g}} A_\Omega(\varphi(|\mathbf{h}|^2))\ \mathbf{f},$$

and conclude from the IFT

$$\begin{aligned} \partial_{\mathbf{f}} \mathbf{g} &= \Pi_{\mathbf{g}} A'_\Omega(\varphi(|\mathbf{h}|^2))(\mathbf{f}) \\ &= \Pi_{\mathbf{g}} [-\partial_{(\mathbf{g},\mathbf{h})} F(\mathbf{f}, (\mathbf{g}, \mathbf{h}))]^{-1} \partial_{\mathbf{f}} F(\mathbf{f}, (\mathbf{g}, \mathbf{h})). \end{aligned}$$

The partial derivatives were computed as follows

$$\partial_{\mathbf{f}} F = -A_\Omega(\varphi(|\mathbf{h}|^2)),$$

and

$$\partial_{\mathbf{g}} F \;=\; \begin{pmatrix} \mathbf{Id}_{I\!R^{2s}} \\ \mathbf{0}_{I\!R^2} \end{pmatrix}.$$

For $\partial_{\mathbf{h}} F$ we have to use Appendix A and the fact that

$$H_\Omega(\varphi(|\mathbf{h}|^2))' = (C_\Omega + D_\Omega\varphi(|\mathbf{h}|^2))' = D_\Omega\ 2\ \varphi'(|\mathbf{h}|^2)\ \langle \mathbf{h}, \cdot \rangle_{I\!R^2}$$

holds.

$$\begin{aligned}
\partial_{\mathbf{h}} F \;&=\; \begin{pmatrix} \mathbf{0}_{I\!R^{2s}} \\ \mathbf{Id}_{I\!R^2} \end{pmatrix} - 2 \begin{pmatrix} \Re(Q_1\partial_{\mathbf{h}} H_\Omega(\varphi(|\mathbf{h}|^2))^{-1}P) & -\Im(Q_1\partial_{\mathbf{h}} H_\Omega(\varphi(|\mathbf{h}|^2))^{-1}P) \\ \Im(Q_1\partial_{\mathbf{h}} H_\Omega(\varphi(|\mathbf{h}|^2))^{-1}P) & \Re(Q_1\partial_{\mathbf{h}} H_\Omega(\varphi(|\mathbf{h}|^2))^{-1}P) \\ \Re(Q_2\partial_{\mathbf{h}} H_\Omega(\varphi(|\mathbf{h}|^2))^{-1}P) & -\Im(Q_2\partial_{\mathbf{h}} H_\Omega(\varphi(|\mathbf{h}|^2))^{-1}P) \\ \Im(Q_2\partial_{\mathbf{h}} H_\Omega(\varphi(|\mathbf{h}|^2))^{-1}P) & \Re(Q_2\partial_{\mathbf{h}} H_\Omega(\varphi(|\mathbf{h}|^2))^{-1}P) \end{pmatrix} \mathbf{f} \\
&=\; \begin{pmatrix} \mathbf{0} \\ \mathbf{Id} \end{pmatrix} + 2 \begin{pmatrix} \Re(Q_1 H_\Omega^{-1} H_\Omega' H_\Omega^{-1}P) & -\Im(Q_1 H_\Omega^{-1} H_\Omega' H_\Omega^{-1}P) \\ \Im(Q_1 H_\Omega^{-1} H_\Omega' H_\Omega^{-1}P) & \Re(Q_1 H_\Omega^{-1} H_\Omega' H_\Omega^{-1}P) \\ \Re(Q_2 H_\Omega^{-1} H_\Omega' H_\Omega^{-1}P) & -\Im(Q_2 H_\Omega^{-1} H_\Omega' H_\Omega^{-1}P) \\ \Im(Q_2 H_\Omega^{-1} H_\Omega' H_\Omega^{-1}P) & \Re(Q_2 H_\Omega^{-1} H_\Omega' H_\Omega^{-1}P) \end{pmatrix} \mathbf{f} \\
&=\; \begin{pmatrix} \mathbf{0} \\ \mathbf{Id} \end{pmatrix} + 4\langle \mathbf{h}, \cdot \rangle_{I\!R^2} \varphi'(|\mathbf{h}|^2) \begin{pmatrix} \Re(Q_1 H_\Omega^{-1} D_\Omega H_\Omega^{-1}P) & -\Im(Q_1 H_\Omega^{-1} D_\Omega H_\Omega^{-1}P) \\ \Im(Q_1 H_\Omega^{-1} D_\Omega H_\Omega^{-1}P) & \Re(Q_1 H_\Omega^{-1} D_\Omega H_\Omega^{-1}P) \\ \Re(Q_2 H_\Omega^{-1} D_\Omega H_\Omega^{-1}P) & -\Im(Q_2 H_\Omega^{-1} D_\Omega H_\Omega^{-1}P) \\ \Im(Q_2 H_\Omega^{-1} D_\Omega H_\Omega^{-1}P) & \Re(Q_2 H_\Omega^{-1} D_\Omega H_\Omega^{-1}P) \end{pmatrix} \mathbf{f}.
\end{aligned}$$

We abbreviate

$$\begin{aligned}
\Pi_{\mathbf{g}} B_\Omega(\varphi(|\mathbf{h}|^2)) \;&:=\; 2 \begin{pmatrix} \Re(Q_1 H_\Omega^{-1} D_\Omega H_\Omega^{-1}P) & -\Im(Q_1 H_\Omega^{-1} D_\Omega H_\Omega^{-1}P) \\ \Im(Q_1 H_\Omega^{-1} D_\Omega H_\Omega^{-1}P) & \Re(Q_1 H_\Omega^{-1} D_\Omega H_\Omega^{-1}P) \end{pmatrix}, \quad (52) \\
\Pi_{\mathbf{h}} B_\Omega(\varphi(|\mathbf{h}|^2)) \;&:=\; 2 \begin{pmatrix} \Re(Q_2 H_\Omega^{-1} D_\Omega H_\Omega^{-1}P) & -\Im(Q_2 H_\Omega^{-1} D_\Omega H_\Omega^{-1}P) \\ \Im(Q_2 H_\Omega^{-1} D_\Omega H_\Omega^{-1}P) & \Re(Q_2 H_\Omega^{-1} D_\Omega H_\Omega^{-1}P) \end{pmatrix}, \\
B_\Omega(\varphi(|\mathbf{h}|^2)) \;&:=\; \begin{pmatrix} \Pi_{\mathbf{g}} B_\Omega(\varphi(|\mathbf{h}|^2)) \\ \Pi_{\mathbf{h}} B_\Omega(\varphi(|\mathbf{h}|^2)) \end{pmatrix},
\end{aligned}$$

and arrive at

$$\Longrightarrow \partial_{(\mathbf{g},\mathbf{h})} F \;=\; \mathbf{Id}_{I\!R^{2s+2}} + \left\langle \begin{pmatrix} \mathbf{0} \\ \mathbf{h} \end{pmatrix}, \cdot \right\rangle 2\varphi'(|\mathbf{h}|^2) B_\Omega(\varphi(|\mathbf{h}|^2))\ \mathbf{f}.$$

As stated in the theorem we have to determine $(\partial_{(\mathbf{g},\mathbf{h})} F)^{-1}$. We use the identity from Appendix B and get

$$(\partial_{(\mathbf{g},\mathbf{h})} F)^{-1} = \mathbf{Id} - \frac{\left\langle \begin{pmatrix} \mathbf{0} \\ \mathbf{h} \end{pmatrix}, \cdot \right\rangle 2\varphi'(|\mathbf{h}|^2) B_\Omega(\varphi(|\mathbf{h})|^2)\mathbf{f}}{1 + 2\varphi'(|\mathbf{h}|^2)\langle \mathbf{h}, \Pi_{\mathbf{h}} B_\Omega(\varphi(|\mathbf{h}|^2))\mathbf{f} \rangle}.$$

So we have $\Pi_{\mathbf{g}} A'_\Omega(\mathbf{f}) = \Pi_{\mathbf{g}} (\partial_{(\mathbf{g},\mathbf{h})} F)^{-1} A_\Omega$ and

$$\Pi_{\mathbf{g}} A'_\Omega(\mathbf{f})\mathbf{v} \;=\; \Pi_{\mathbf{g}} A_\Omega \mathbf{v} - 2\varphi'(|\mathbf{h}|^2) \frac{\langle \mathbf{h}, \Pi_{\mathbf{h}} A_\Omega \mathbf{v}\rangle}{1 + 2\varphi'(|\mathbf{h}|^2)\langle \mathbf{h}, \Pi_{\mathbf{h}} B_\Omega \mathbf{f}\rangle} \Pi_{\mathbf{g}} B_\Omega \mathbf{f}. \qquad \square$$

Next we want to compute the adjoint of the derivative.

Lemma 3 *Each component of the adjoint $A'(f)^*$ of $A'(f)$ given in (50) is computed by*

$$[\Pi_{\mathbf{g}} A'_\Omega(\mathbf{f})]^* = [\Pi_{\mathbf{g}} A_\Omega]^* - 2\varphi'(|\mathbf{h}|^2) \frac{[\Pi_{\mathbf{h}} A_\Omega]^* \mathbf{h}}{1 + 2\varphi'(|\mathbf{h}|^2)\langle \Pi_{\mathbf{h}} B_\Omega \mathbf{f}, \mathbf{h}\rangle} \langle \Pi_{\mathbf{g}} B_\Omega \mathbf{f}, \cdot \rangle. \qquad (53)$$

Proof: We have

$$\begin{aligned}
& \langle [\Pi_{\mathbf{g}} A'_\Omega(\mathbf{f})]^* \mathbf{w}, \mathbf{v}\rangle \\
= \;& \langle \mathbf{w}, \Pi_{\mathbf{g}} A'_\Omega(\mathbf{f})\mathbf{v}\rangle \\
= \;& \langle \mathbf{w}, \Pi_{\mathbf{g}} A_\Omega \mathbf{v}\rangle - 2\varphi'(|\mathbf{h}|^2) \left\langle \mathbf{w}, \frac{\langle \mathbf{h}, \Pi_{\mathbf{h}} A_\Omega \mathbf{v}\rangle}{1 + 2\varphi'(|\mathbf{h}|^2)\langle \mathbf{h}, \Pi_{\mathbf{h}} B_\Omega \mathbf{f}\rangle} \Pi_{\mathbf{g}} B_\Omega \mathbf{f} \right\rangle \\
= \;& \langle [\Pi_{\mathbf{g}} A_\Omega]^* \mathbf{w}, \mathbf{v}\rangle - 2\varphi'(|\mathbf{h}|^2) \left\langle \frac{\langle \Pi_{\mathbf{g}} B_\Omega \mathbf{f}, \mathbf{w}\rangle}{1 + 2\varphi'(|\mathbf{h}|^2)\langle \Pi_{\mathbf{h}} B_\Omega \mathbf{f}, \mathbf{h}\rangle} [\Pi_{\mathbf{h}} A_\Omega]^* \mathbf{h}, \mathbf{v} \right\rangle. \qquad \square
\end{aligned}$$

We remark that in order to compute $A'(f)^*$, we also need to table the matrices

$$\begin{pmatrix} \Re(Q_1 H_\Omega(\varphi'(|\mathbf{h}_i|^2)^{-1} D_\Omega H_\Omega(\varphi'(|\mathbf{h}_i|^2)^{-1} P) & \Im(Q_1 H_\Omega(\varphi'(|\mathbf{h}_i|^2)^{-1} D_\Omega H_\Omega(\varphi'(|\mathbf{h}_i|^2)^{-1} P) \\ \Re(Q_2 H_\Omega(\varphi'(|\mathbf{h}_i|^2)^{-1} D_\Omega H_\Omega(\varphi'(|\mathbf{h}_i|^2)^{-1} P) & \Im(Q_2 H_\Omega(\varphi'(|\mathbf{h}_i|^2)^{-1} D_\Omega H_\Omega(\varphi'(|\mathbf{h}_i|^2)^{-1} P) \end{pmatrix},$$

$i = 1, \cdots, I_{max}$, from which we construct the matrix B_Ω otherwise the computation of $A'(f)^*$ would be impossible.
If the derivative is known, gradient based methods are easily implemented.

5.2 On the minimization of the Tikhonov functional

For the numerical realization of the Tikhonov regularization the minimizer

$$f_\alpha^\delta := \arg\min_f J_\alpha(f)$$

has to be computed. For a linear operator A, this is simply done by solving the linear system

$$(A^*A + \alpha I) f = A^* g^\delta + \alpha \bar{f} \ .$$

For nonlinear operator A this demands more. At first, the minimizer of the Tikhonov functional might not be unique anymore, and there might be even only local minimizers. Secondly, the Tikhonov functional is no longer convex. This

means in particular that classical algorithms like the steepest descent method can fail to converge to a global minimizer. In [10, 11] the so called TIGRA (TIkhonov–GRAdient)–algorithm was proposed. This method is a combination of Tikhonov regularization and a gradient method for the minimization of the Tikhonov functional. The basic algorithm is as follows:

- Given g^δ with $\|g^\delta - g\| \leq \delta$
- Choose $\alpha_0,\ q < 1$,
- **Repeat**

  $k = k + 1$

  $\alpha_k = q^k \alpha_0$

  Compute $f^\delta_{\alpha_k} = \arg\min J_{\alpha_k}(f)$ with the gradient method

  until $\|A f^\delta_{\alpha_k} - g^\delta\|^2 \leq c\delta^2$

Under slight restrictions to the nonlinear operator A it has been shown [11] that this algorithm reconstructs a good approximation to a $\bar{f}$–minimum–norm–solution f^* of $A\,f = g$, provided α_0 and q are chosen appropriately and

$$\bar{f} - f^* = A'(f^*)^*\,\omega$$

with $\|\omega\|$ small enough holds. In this case, an error estimate of the form

$$\|f^\delta_{\alpha_k} - f^*\| = O(\sqrt{\delta}) \tag{54}$$

holds. We have used the TIGRA–algorithm for several reconstructions, but found the algorithm rather slow in convergence, which was mainly due to the high number of iterations for the gradient method required for the minimization of the Tikhonov functional for each α_k. Thus, our focus was on a replacement of the gradient method by a faster algorithm. First, we want to show that every minimizer of the Tikhonov functional can be characterized as a fixed point of the mapping Φ defined in the following Lemma.

Lemma 4 *Every minimizer of the Tikhonov functional fulfills the fixed point equation*

$$f = \Phi(f) \qquad \textit{with} \tag{55}$$

$$\Phi(f) := T_\alpha(f)^{-1}\left(A'(f)^* g^\delta + \alpha \bar{f}\right). \tag{56}$$

Proof: The necessary condition for a minimum of $J_\alpha(f)$ reads (see (25))

$$\alpha(f - \bar{f}) = A'(f)^*(g^\delta - Af)\ ,$$

which is equivalent to

$$(A'(f)^*A + \alpha I)f = A'(f)^*g^\delta + \alpha\bar{f}. \tag{57}$$

According to (50), $A'(f)^*$ is a $(2N \times 2s \cdot K)$–matrix. By (42) we find that the data $g = Af$ are given by

$$Af = \Pi_{\mathbf{g}} \begin{pmatrix} A_{\Omega_1}(\varphi(|h|^2)) \\ \vdots \\ A_{\Omega_K}(\varphi(|h|^2)) \end{pmatrix} \mathbf{f} \ , \tag{58}$$

with $h = h(f)$. Looking at (50), we see that for given $|h|^2$, A is a $(2s \cdot K \times 2N)$–matrix, and $A'(f)^*A(\varphi(|h|^2))$ is a $(2N \times 2N)$–matrix.
By the methods presented in Section 4.2 we can compute

$$A'(f)^*A(\varphi(|h|^2))\ f = \Pi_{\mathbf{g}} \left(\ A'_{\Omega_1}(\mathbf{f})^* \dots A'_{\Omega_K}(\mathbf{f})^* \ \right) \Pi_{\mathbf{g}} \begin{pmatrix} A_{\Omega_1}(\varphi(|h|^2)) \\ \vdots \\ A_{\Omega_K}(\varphi(|h|^2)) \end{pmatrix} \mathbf{f}$$

for every given $f = \mathbf{f}$, and thus the matrix

$$T_\alpha(f) = A'(f)^*A(\varphi(|h|^2)) + \alpha I \tag{59}$$

is well defined, and equation (57) is equivalent to

$$f = \Phi(f) := T_\alpha(f)^{-1} \left(A'(f)^*g^\delta + \alpha\bar{f} \right) \ . \qquad \square$$

We remark that the belonging iteration $f_{k+1} = \Phi(f_k)$ converged very fast to a minimizer of the Tikhonov functional.

5.3 Reconstruction algorithm

Applying Morozov's discrepancy principle, our resulting algorithm reads as follows:

- Given g^δ with $\|g^\delta - g\| \le \delta$
- Choose $\alpha_0,\ q < 1,\ tol$ and f_0, f_1 with $\|f_1 - f_0\|^2/\|f_1\|^2 > tol,\ k = 0$
- **Repeat**
  - $k = k + 1$
  - $\alpha_k = q^k \alpha_0$
  - **While** $\|f_1 - f_0\|^2/\|f_1\|^2 > tol$
    - find$A(f_0)$ for f_0 by computing the zero of (45)
    - $f_1 = (A'(f_0)^*A(f_0) + \alpha_k I)^{-1}(A'(f_0)^*g^\delta + \alpha_k\bar{f})$
  - **end**
  - $f_0 = f_1$

  until $\|A(f_0)f_0 - g^\delta\|^2 \le \delta^2$

A reconstruction of an unbalance distribution from noisy data with the above algorithm needed in average less than two minutes (Matlab implementation, on a PC with 1.33 GHz AMD processor). In comparison, the TIGRA–algorithm needed about an hour for a full reconstruction. As we will see in the following Section, the above algorithm did always converge. A convergence analysis of the algorithm is not the scope of the present work but will be the topic of a forthcoming paper.

6 Reconstruction results

We have performed a large number of test computations using the following model parameters:

- $s = 5$ sensor positions at the housing [squeeze film damper(1), bearing with constant damping(5), and (2,3,4) equidistantly distributed between (1) and (5)]
- $N = 10$ sources of unbalances (compressor: eccentricities at the discs 1 to 6, turbine: eccentricities at the discs 7 and 8, coupling: run out 9, and swash 10)
- $K = 60$ frequencies $[5, 10, 15, \ldots, 300]Hz$
- a sample of $I_{max} = 30$ values for $|h|^2/H^2$:
  $[0, 0.01, 0.02, \ldots, 0.08, 0.1, 0.15, 0.2, \ldots, 0.95, 0.99, 0.999, 0.9999]$

Given an unbalance or an unbalance distribution, the data $\mathbf{g}^\delta$ were produced by forward computation and disturbed with a random additive error of 5% and a random multiplicative error of 15%. For $\bar{\mathbf{f}}$ we have always chosen the zero vector.

6.1 Reconstruction of a single unbalance

First, we have tested our program for several single given unbalances $\mathbf{f}$, namely for an eccentricity at the 2nd disc in the compressor ($f(2) = 0.05mm$), one at the 7th disc in the turbine ($f(7) = 0.05mm$), and a run out of the coupling ($f(9) = 0.02mm$).

6.1.1 First reconstruction results

We have plotted our reconstruction results in the Figures 15 to 17. The first picture (top left) always shows the reference unbalance $\mathbf{f}$, the second (top right) its vibration impact at the damper sensor position. In the third picture (lower

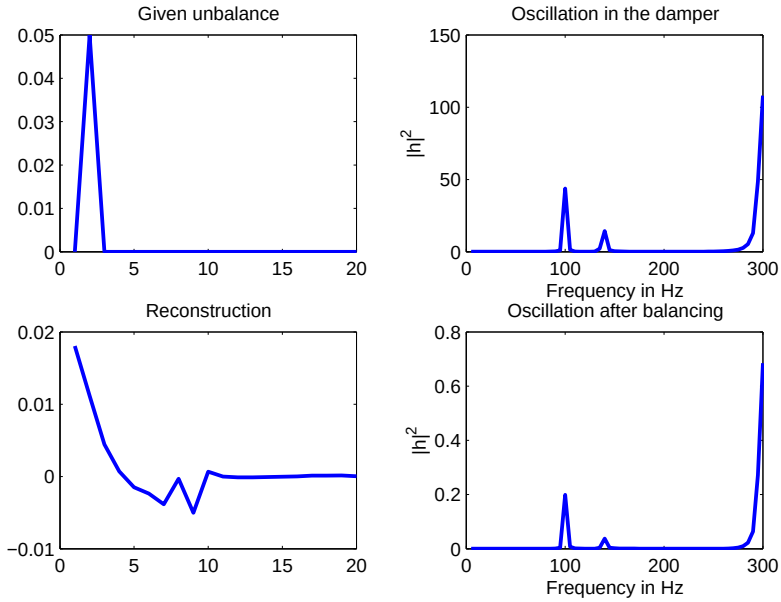

Figure 15: Unbalance at 2nd disc (compressor): reconstruction results

left) the reconstructed unbalance distribution $\mathbf{f}_{rec}$ is plotted, and finally picture four (lower right) shows the vibration at the damper sensor position after balancing, i.e. we imagined to place balancing masses according to the reconstructed distribution, meaning we did a forward computation with $\mathbf{f} - \mathbf{f}_{rec}$. Although the results give a hint where the unbalances are situated, the algorithm fails to reconstruct the original unbalance. The reason lies in the following facts. Due to the nature of the measurement process we are working with incomplete data. It is a well known fact from the linear theory of rotor dynamic systems that most information is contained in the resonance frequencies. There are the same number of resonance frequencies as the number of knots in the model, but usually only first the ten to fifteen of them are physically reasonable. Using a frequency interval containing all reasonable resonance frequencies, we expect the inverse problem to have a unique solution. However, in practice it is impossible to obtain measurements for all reasonable resonance frequencies and we had to restrict ourselves to an interval that contained two and approaches a third resonance frequency. Different unbalance distributions may produce different vibrations at the sensors within an interval containing all resonance frequencies, but may coincide on the considered subinterval. Thus we have lost the uniqueness of the solution of the inverse problem. Tikhonov regularization with a given $\bar{\mathbf{f}}$ reconstructs then a solution closest to $\bar{\mathbf{f}}$. In our case with $\bar{\mathbf{f}} = \mathbf{0}$, this means that we end up with a reconstruction for the cause of the unbalance with minimal mass, as can be seen in the Figures 15 to 17. Although the balancing results are very good, in practice we want to have as less balancing positions as possible due to the costs of the balancing process. Hence the computed reconstructions are not satisfying. To achieve a reconstruction that coincides with the given unbalance we want to locate

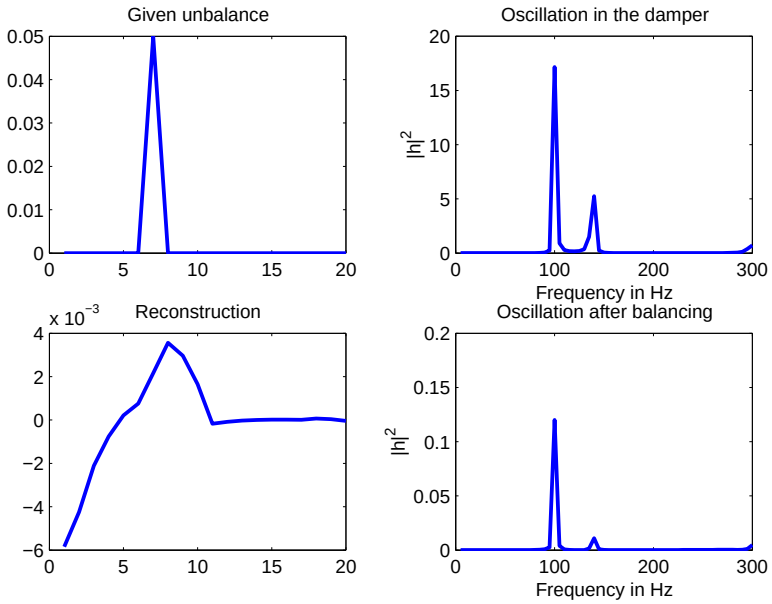

Figure 16: Unbalance at 7th disc (turbine): reconstruction results

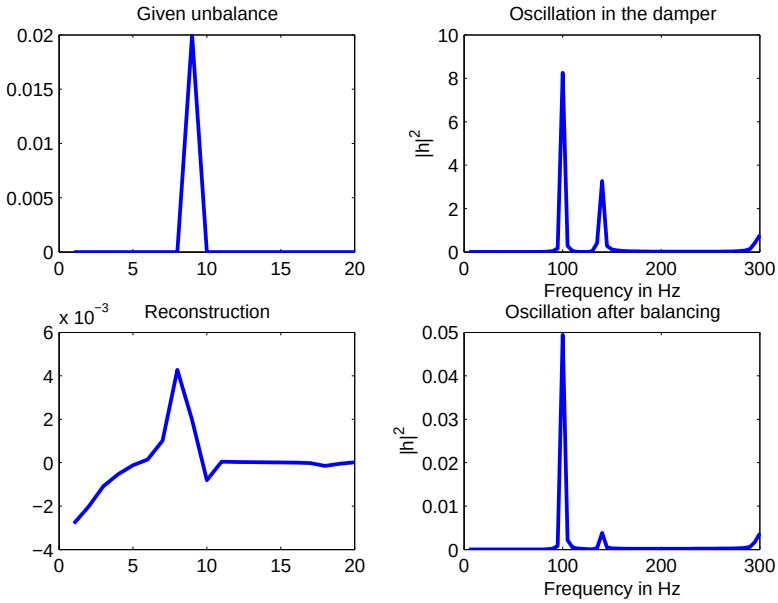

Figure 17: Run out in the coupling: reconstruction results

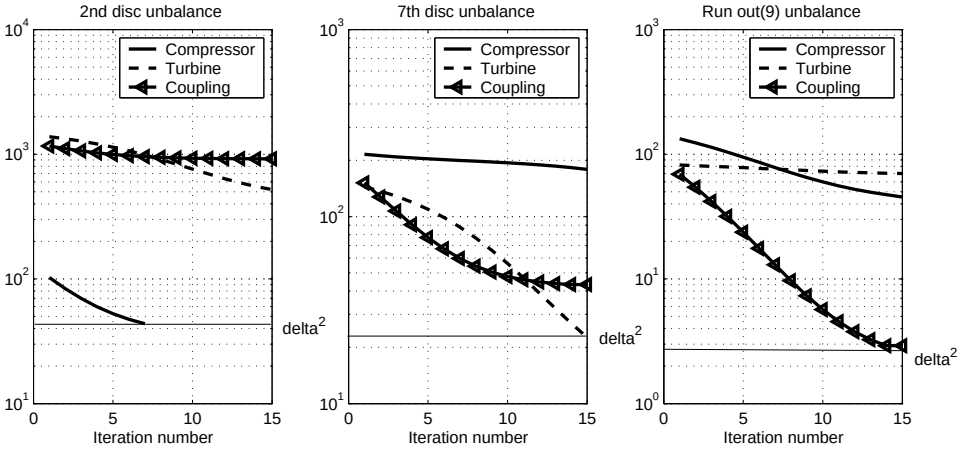

Figure 18: Residua $\|A_i \mathbf{f}_\alpha^\delta - g^\delta\|^2$ for compressor, turbine and coupling part, indicating the location of a causing unbalance

its position first. To this end we have defined an operator $A_{[i_1,\ldots,i_m]},\ i_m \in [1, N]$, which is a restriction of A to the unbalance positions indicated by $i_1, \ldots, i_m$, i.e. this operator allows only an unbalance reconstruction at the given positions. These operators can be obtained by extracting the corresponding columns of the matrices A in (50).

6.1.2 Locating of unbalances in compressor, turbine and coupling

As stated above we want to identify the part of the engine (compressor $= [1, \ldots, 6]$, turbine $= [7, 8]$ or coupling $= [9, 10]$) where the causing unbalance is located. Since we assume that we have single unbalance causes, we can only expect reasonable reconstructions with one of the operators A_{comp}, A_{turb} and A_{coup}. According to the theory of Tikhonov regularization, a necessary condition for a good reconstruction is that the residual $\|A\mathbf{f}_\alpha^\delta - \mathbf{g}^\delta\|$ is of the same magnitude as the data error δ. As we can see in Figure 18, we equal the data error level only with one of the restricted operators while the residua of the others stagnated on a higher level, and conclude that the unbalance can be located only in the part of the engine where the residual with the restricted operator approaches δ.

6.1.3 Locating of a single unbalance position

Once the unbalance causing part of the engine is located, we scan through the possible unbalance positions in order to find the positions where the residuum $\|A_{[i]}\mathbf{f}_{\alpha,[i]}^\delta - g^\delta\|$ equals δ. For example, for the 2nd disc unbalance we did reconstructions with $A_{[1]}, \cdots, A_{[6]}$. Only by using $A_{[2]}$ the residuum equals δ, indicating that the unbalance position has been found. With the belonging reconstruction

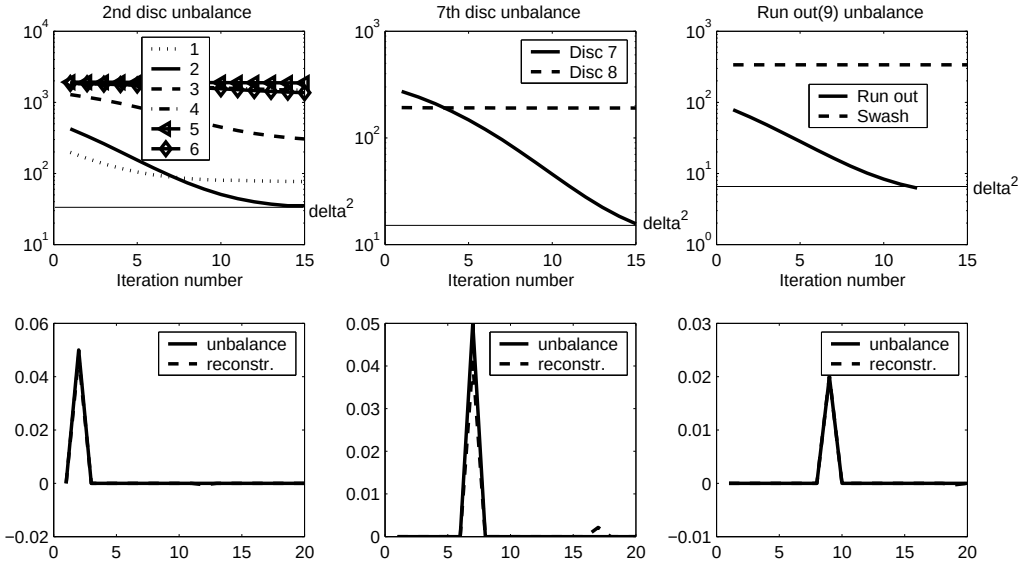

Figure 19: Identification of unbalance positions in the parts of the engine; residua for the single positions (top), and original and reconstructed unbalance (lower)

$\mathbf{f}^{\delta}_{\alpha,[2]}$, the relative reconstruction error $\|\mathbf{f}^{\delta}_{\alpha,[2]} - \mathbf{f}\|/\|\mathbf{f}\|$ was about 5%. Similar results hold for the other single unbalances, see Figure 19.

6.1.4 General reconstruction approach

The results of the preceding subsections suggest the following general approach to reconstruct a single unbalance:

1. Do a minimum–norm reconstruction according to subsection 6.1.1 in order to check the magnitude of the residuum and possible balancing results.
2. Identify the part of the rotor where the unbalance is located choosing the part for which the residuum equals δ (cf. subsection 6.1.2).
3. Scan through the identified part allowing only single unbalance positions for the reconstruction. Again choose the position where the residuum equals δ (cf. subsection 6.1.3).

6.2 Reconstruction of an unbalance distribution

To reconstruct an unbalance distribution we have also used the above suggested approach. During this section we have chosen an eccentricity of 0.05 mm at the third disc in the compressor and a run out error of 0.02 mm in the coupling. We made a minimum norm reconstruction **first** in order to get an impression which

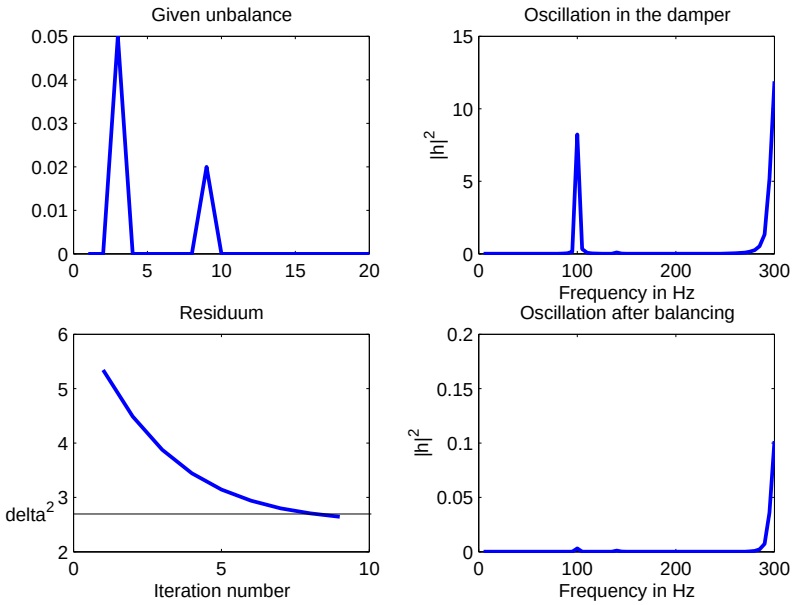

Figure 20: Reconstruction residuum (lower left) and balancing result (lower right compared to upper right) for an unbalance distribution (upper left)

reconstruction and balancing accuracy is possible (Figure 20). In a **second** step we compared the residua of the iteration process restricted to the three single parts and combinations of two parts of the engine (Figure 21). As a conclusion of Figure 21 we presume our unbalances either in the compressor and the turbine or in the compressor and the coupling. It is not very surprising that we can not identify only one combination since, for instance, the 7th disc in the turbine is close to the coupling and a balancing weight there will probably have a satisfying effect on the considered frequency interval.
This time the **third** step is parted. We first allow only single potential unbalance positions and compute the residua (Figure 22). We can see that non of the residua comes near δ. But when we are looking for a combination of the compressor and one of the other parts, Figure 22 recommends to try the positions of disc 1, 2, 3 and 6, since there a decreasing of the residuum is visible. Thus we checked the residua for the restricted operators $A_{[i,7]}, \cdots, A_{[i,10]}, i = 1, 2, 3, 6$ and plotted the results in Figure 23. Though some of the combinations residua came close to δ, only the right combination residuum $\|A_{[3,9]}\ \mathbf{f}_\alpha^\delta - \mathbf{g}^\delta\|$ undercut the δ–level and the iteration stopped. The other residua remained static at a slightly higher level. For the last iterate of the most recommended combinations, we have the following residua ($\delta^2 = 2.68$):

$$\begin{aligned}
\|A_{[3,9]}\ \mathbf{f}_\alpha^\delta - \mathbf{g}^\delta\|^2 &= 2.66 \\
\|A_{[1,7]}\ \mathbf{f}_\alpha^\delta - \mathbf{g}^\delta\|^2 &= 3.87 \\
\|A_{[2,7]}\ \mathbf{f}_\alpha^\delta - \mathbf{g}^\delta\|^2 &= 4.29 \\
\|A_{[3,8]}\ \mathbf{f}_\alpha^\delta - \mathbf{g}^\delta\|^2 &= 3.17
\end{aligned}$$

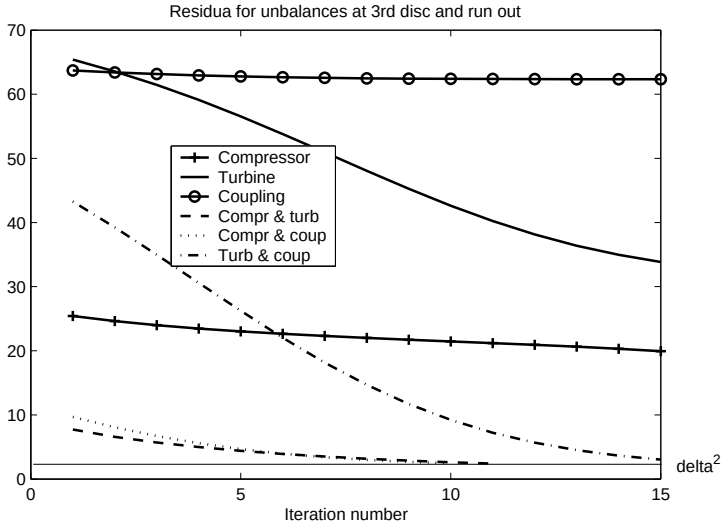

Figure 21: Localization of the parts for an unbalance distribution

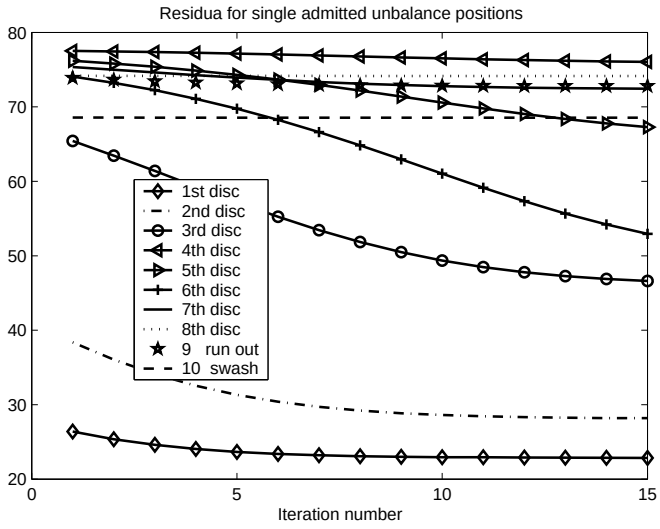

Figure 22: Residua squares for the 10 single potential unbalance positions

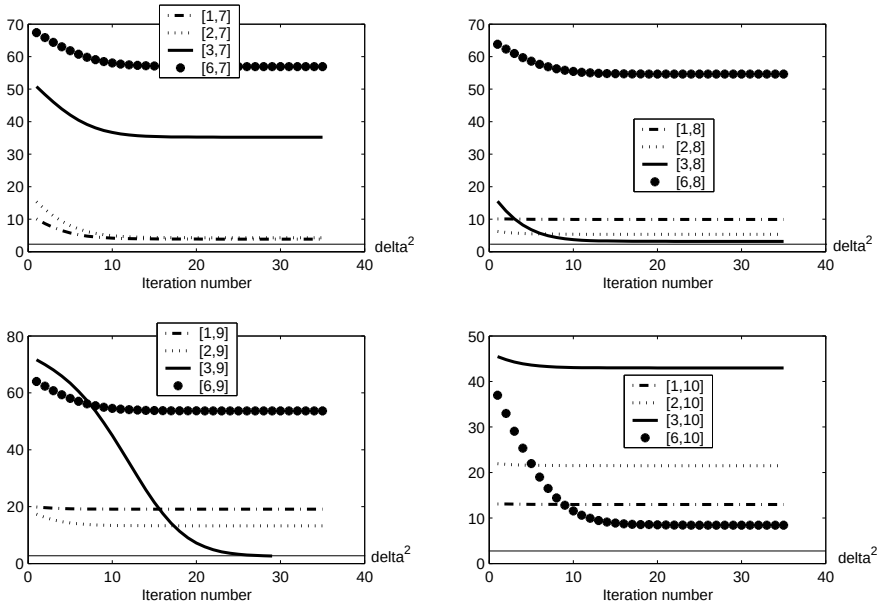

Figure 23: Residua squares for combinations of two potential unbalance positions; disc 1,2,3 and 6 from the compressor with the remaining positions 7 and 8 from the turbine, and 9 and 10 from the coupling

We have to remark that in our case δ is exactly known. For reconstructions with real data, δ has to be estimated. Therefor it is possible that more than one combination undercut the estimated δ–level. But due to the regularization theory, the residuum for the right combination tends to zero if α tends to zero. As we can see in Figure 23, the wrong combinations remain almost static. The reconstructed unbalance distribution and the balancing result for $A_{[3,9]}$ can be seen in Figure 24. The relative reconstruction error $\|\mathbf{f}^{\delta}_{\alpha,[3,9]} - \mathbf{f}\|/\|\mathbf{f}\|$ is about 7%.

6.3 Balancing at three fixed positions

Sometimes one is not or not only interested in the identification of an unbalance distribution but in good balancing results. In practice one often has three fixed positions where balancing weights can be placed. We assumed disc 1, 5 and 8 as such fixed positions and computed the corresponding solution $\mathbf{f}^{\delta}_{\alpha,[1,5,8]}$ and the balancing result (see Figure 25) for the data generated by the above unbalance distribution $[3, 9]$. We can see that the residuum $\|A_{[1,5,8]}\ \mathbf{f}^{\delta}_{\alpha,[1,5,8]} - \mathbf{g}^{\delta}\|^2$ equals δ much faster than the residuum of the $A_{[3,9]}$–reconstruction (see Figure 24). Also the balancing results are much better. For our three–point balancing we got a remaining oscillation in the squeeze film damper of less than 0.3%.

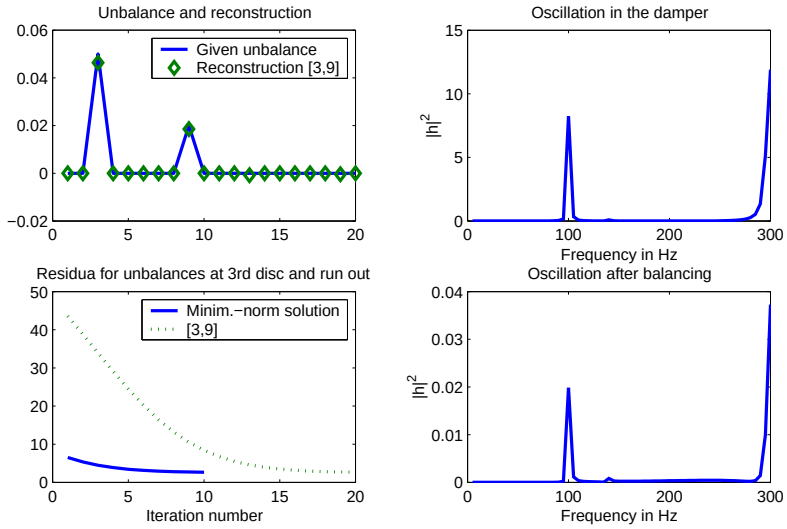

Figure 24: Reconstruction results for $A_{[3,9]}$

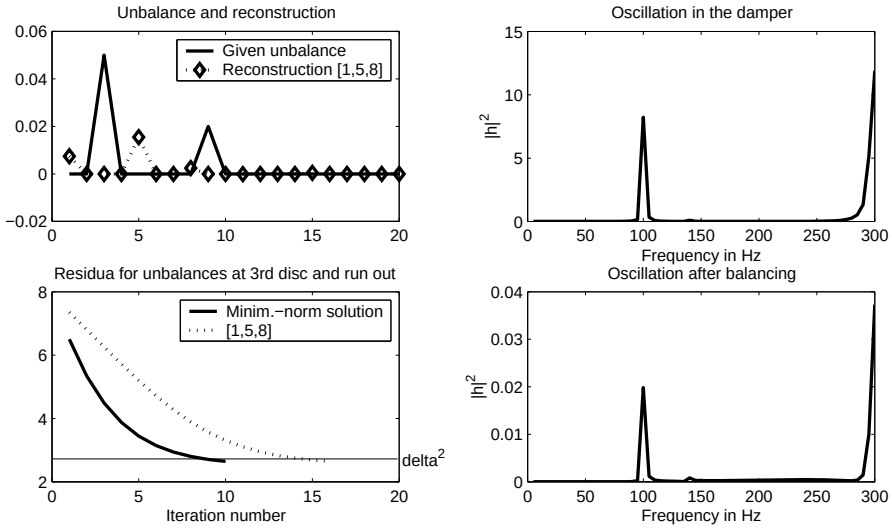

Figure 25: Reconstruction results for $A_{[1,5,8]}$

6.4 Data error and reconstruction quality

Surely an important item for the unbalance identification accuracy is the quality of the available data. Since we did not have access to real data, we had to revert to simulated data. We have used a reference unbalance at the third disc ($\mathbf{f}(3) = 0.05$), produced the corresponding data by forward computation and disturbed the data with equally distributed random numbers normed to the error level. We varied the error level from 0% to 50%, and applied our three–step algorithm. There was no difficulty to identify the engine's unbalanced parts and finally the unbalance position. The reconstructed solution $\mathbf{f}_{rec}$ was computed using the operator restricted to the 3rd unbalance position $A_{[3]}$. We defined two measures for the accuracy. The first one is the identification accuracy.

$$\text{Identification accuracy } = \left(1 - \frac{\|\mathbf{f} - \mathbf{f}_{rec}\|}{\|\mathbf{f}\|}\right) * 100\%.$$

Its dependence on the data error level is plotted in the left picture of Figure 26. For exact data, the unbalance is exactly reconstructed. The second accuracy measure considers the balancing effect. We compared the oscillation $|h|^2$ in the squeeze film damper caused by the reference unbalance with the oscillation after balancing with the reconstructed solution $|h_{rec}|^2$ (i.e. forward computation with $\mathbf{f} - \mathbf{f}_{rec}$). The balancing accuracy was defined by

$$\text{Balancing accuracy } = \left(1 - \frac{|h_{rec}|^2}{|h|^2}\right) * 100\%.$$

The right picture of Figure 26 shows the dependence on the data error level. For exact data we have 100% accuracy, i.e. no remaining unbalance after balancing. For 50% data error we have less than 15% remaining unbalance.

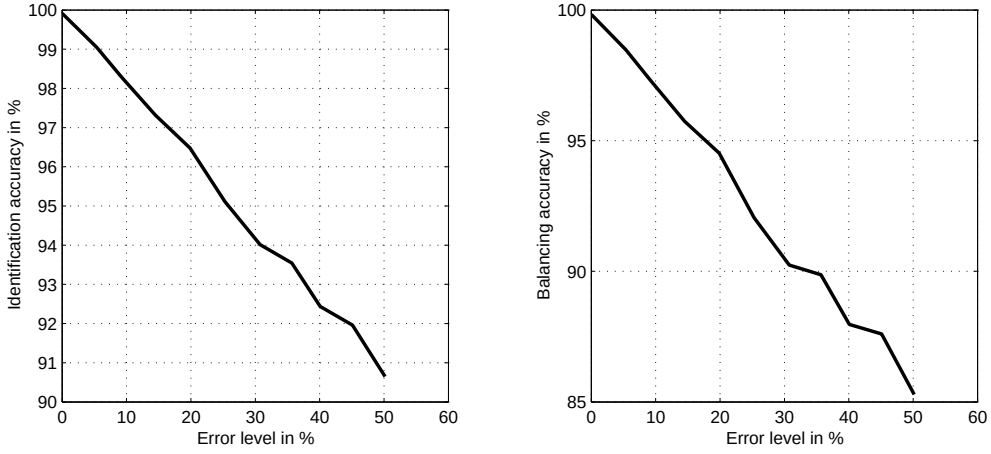

Figure 26: Identification and balancing accuracy versus noise level

7 Summary

We have developed a nonlinear turbine model oriented on the characteristic parameters of a real engine. It has enabled us to compute the oscillation behavior of the turbine from given unbalance distributions. Based on this model and on the Tikhonov regularization for nonlinear ill–posed problems, we have introduced a three-step algorithm to reconstruct unbalances in the engine from noisy data measured at certain sensor positions on the engine's casing. For the first time, point unbalances and discontinuous unbalance distributions could be exactly localized and reconstructed with satisfying accuracy. Additionally, if balancing positions are previously fixed, the step algorithm enables us to compute balancing masses with very good balancing results.
The treatment of model errors and a comparison of the linear and the nonlinear model were also under investigation and are topics of a forthcoming paper.

A Derivative of an inverse matrix

Suppose we want to determine $[B(\varphi)^{-1}]'$. We use the Taylor expansion of $B(\varphi+\varepsilon)^{-1}$ to determine the derivative from

$$B(\varphi+\varepsilon)^{-1} = B(\varphi)^{-1} + [B(\varphi)^{-1}]'\varepsilon + R(\varepsilon^2).$$

First we have

$$B(\varphi+\varepsilon)^{-1} = [B(\varphi) + [B(\varphi)]'\varepsilon + R(\varepsilon^2)]^{-1}.$$

Here $[B(\varphi)]'\varepsilon = E\varepsilon$ is a small term and $R(\varepsilon^2)$ is 'very small'. We have to determine $(B+\varepsilon E + R(\varepsilon^2))^{-1}$. This can be done by the following chain where we use the Neumann serie $(Id-A)^{-1} = \sum_{k=0}^{\infty} A^k$.

$$\begin{aligned}
(B+\varepsilon E + R(\varepsilon^2))^{-1} &= [B(Id - (-\varepsilon B^{-1}E) + B^{-1}R(\varepsilon^2))]^{-1} \\
&= [Id - (-\varepsilon B^{-1}E) + R_1(\varepsilon^2)]^{-1}B^{-1} \\
&= \sum_{k=0}^{\infty}(-\varepsilon B^{-1}E + R_1(\varepsilon^2))^k B^{-1} \\
&= B^{-1} - \varepsilon B^{-1}EB^{-1} + R_2(\varepsilon^2).
\end{aligned}$$

It follows that

$$B(\varphi+\varepsilon)^{-1} = B(\varphi)^{-1} - \varepsilon B(\varphi)^{-1}[B(\varphi)]'B(\varphi)^{-1} + R_2(\varepsilon^2),$$

hence

$$[B(\varphi)^{-1}]' = -B(\varphi)^{-1}[B(\varphi)]'B(\varphi)^{-1}.$$

B

We want to proof

$$(Id + \langle q, \cdot\rangle w)^{-1} = Id - \frac{1}{1+\langle q, w\rangle}\langle q, \cdot\rangle w.$$

Since $\langle q, \cdot\rangle w = wq^t$ and $wq^twq^t = wq^t\langle q, w\rangle$ we have

$$\begin{aligned}
(Id + wq^t)(Id - cwq^t) &= Id + wq^t - cwq^t - cwq^twq^t \\
&= Id + wq^t(1 - c - c\langle q, w\rangle) \\
&= Id \\
&\Leftrightarrow\ 1 - c - c\langle q, w\rangle = 0 \\
&\Leftrightarrow\ c = \frac{1}{1+\langle q, w\rangle}.
\end{aligned}$$

References

[1] R. D. Blevins. *Formulas for Natural Frequency and Mode Shape*. van Nostrand Reinhold, New York, 1979.

[2] V. Dicken. Inverse Imbalance Reconstruction in Rotordynamics. *CERES report on the ZeTeM subcontract for Task 6.2.*, 2001.

[3] H. W. Engl, M. Hanke, and A. Neubauer. *Regularization of Inverse Problems*. Kluwer, Dordrecht, 1996.

[4] R. Gasch and K. Knothe. *Strukturdynamik Bd.2 Kontinua und ihre Diskretisierung*. Springer, Berlin, 1989.

[5] R. Gasch, R. Nordmann, and H. Pfützner. *Rotordynamik*. Springer, Berlin, 2002.

[6] R. Holmes. Rotor vibration control using squeeze film dampers. *IFToMM, Fifth International Conference on Rotordynamics*, 1998.

[7] K. Knothe and H. Wessls. *Finite Elemente - eine Einführung für Ingenieure*. Springer, Berlin, 1992.

[8] A. K. Louis. *Inverse und schlecht gestellte Probleme*. Teubner, Stuttgart, 1989.

[9] R. Ramlau. Morozov's discrepancy principle for Tikhonov regularization of nonlinear operators. *Numer. Funct. Anal. and Optimiz*, 23(1&2):147–172, 2002.

[10] R. Ramlau. A steepest descent algorithm for the global minimization of the Tikhonov– functional. *Inverse Problems*, 18(2):381–405, 2002.

[11] R. Ramlau. TIGRA–an iterative algorithm for regularizing nonlinear ill–posed problems. *Inverse Problems*, 19(2):433–467, 2003.

[12] A. Rienäcker, D. Peters, G. Tokar, and B. Domes. Einsatz inverser Methoden zur Bestimmung der Rotorunwuchtverteilung eines Flugtriebwerks. *VDI Berichte: Schwingungsüberwachung und -diagnose von Maschinen und Anlagen: Tagung Frankenthal, 27./28. Mai 1999*, (1466):363–373, 1999.

[13] O. Scherzer. The use of Morozov's discrepancy principle for Tikhonov regularization for solving nonlinear ill–posed problems. *Computing*, (51):45–60, 1993.

Berichte aus der Technomathematik ISSN 1435-7968

http://www.math.uni-bremen.de/zetem/berichte.html

— Vertrieb durch den Autor —

Reports **Stand: 24. Juli 2003**

98–01. Peter Benner, Heike Faßbender:
An Implicitly Restarted Symplectic Lanczos Method for the Symplectic Eigenvalue Problem, Juli 1998.

98–02. Heike Faßbender:
Sliding Window Schemes for Discrete Least-Squares Approximation by Trigonometric Polynomials, Juli 1998.

98–03. Peter Benner, Maribel Castillo, Enrique S. Quintana-Ortí:
Parallel Partial Stabilizing Algorithms for Large Linear Control Systems, Juli 1998.

98–04. Peter Benner:
Computational Methods for Linear–Quadratic Optimization, August 1998.

98–05. Peter Benner, Ralph Byers, Enrique S. Quintana-Ortí, Gregorio Quintana-Ortí:
Solving Algebraic Riccati Equations on Parallel Computers Using Newton's Method with Exact Line Search, August 1998.

98–06. Lars Grüne, Fabian Wirth:
On the rate of convergence of infinite horizon discounted optimal value functions, November 1998.

98–07. Peter Benner, Volker Mehrmann, Hongguo Xu:
A Note on the Numerical Solution of Complex Hamiltonian and Skew-Hamiltonian Eigenvalue Problems, November 1998.

98–08. Eberhard Bänsch, Burkhard Höhn:
Numerical simulation of a silicon floating zone with a free capillary surface, Dezember 1998.

99–01. Heike Faßbender:
The Parameterized SR Algorithm for Symplectic (Butterfly) Matrices, Februar 1999.

99–02. Heike Faßbender:
Error Analysis of the symplectic Lanczos Method for the symplectic Eigenvalue Problem, März 1999.

99–03. Eberhard Bänsch, Alfred Schmidt:
Simulation of dendritic crystal growth with thermal convection, März 1999.

99–04. Eberhard Bänsch:
Finite element discretization of the Navier-Stokes equations with a free capillary surface, März 1999.

99–05. Peter Benner:
Mathematik in der Berufspraxis, Juli 1999.

99–06. Andrew D.B. Paice, Fabian R. Wirth:
Robustness of nonlinear systems and their domains of attraction, August 1999.

99–07. Peter Benner, Enrique S. Quintana-Ortí, Gregorio Quintana-Ortí:
Balanced Truncation Model Reduction of Large-Scale Dense Systems on Parallel Computers, September 1999.

99–08. Ronald Stöver:
Collocation methods for solving linear differential-algebraic boundary value problems, September 1999.

99–09. Huseyin Akcay:
Modelling with Orthonormal Basis Functions, September 1999.

99–10. Heike Faßbender, D. Steven Mackey, Niloufer Mackey:
Hamilton and Jacobi come full circle: Jacobi algorithms for structured Hamiltonian eigenproblems, Oktober 1999.

99–11. Peter Benner, Vincente Hernández, Antonio Pastor:
On the Kleinman Iteration for Nonstabilizable System, Oktober 1999.

99–12. Peter Benner, Heike Faßbender:
A Hybrid Method for the Numerical Solution of Discrete-Time Algebraic Riccati Equations, November 1999.

99–13. Peter Benner, Enrique S. Quintana-Ortí, Gregorio Quintana-Ortí:
Numerical Solution of Schur Stable Linear Matrix Equations on Multicomputers, November 1999.

99–14. Eberhard Bänsch, Karol Mikula:
Adaptivity in 3D Image Processing, Dezember 1999.

00–01. Peter Benner, Volker Mehrmann, Hongguo Xu:
Perturbation Analysis for the Eigenvalue Problem of a Formal Product of Matrices, Januar 2000.

00–02. Ziping Huang:
Finite Element Method for Mixed Problems with Penalty, Januar 2000.

00–03. Gianfrancesco Martinico:
Recursive mesh refinement in 3D, Februar 2000.

00–04. Eberhard Bänsch, Christoph Egbers, Oliver Meincke, Nicoleta Scurtu:
Taylor-Couette System with Asymmetric Boundary Conditions, Februar 2000.

00–05. Peter Benner:
Symplectic Balancing of Hamiltonian Matrices, Februar 2000.

00–06. Fabio Camilli, Lars Grüne, Fabian Wirth:
A regularization of Zubov's equation for robust domains of attraction, März 2000.

00–07. Michael Wolff, Eberhard Bänsch, Michael Böhm, Dominic Davis:
Modellierung der Abkühlung von Stahlbrammen, März 2000.

00–08. Stephan Dahlke, Peter Maaß, Gerd Teschke:
Interpolating Scaling Functions with Duals, April 2000.

00–09. Jochen Behrens, Fabian Wirth:
A globalization procedure for locally stabilizing controllers, Mai 2000.

00–10. Peter Maaß, Gerd Teschke, Werner Willmann, Günter Wollmann:
Detection and Classification of Material Attributes – A Practical Application of Wavelet Analysis, Mai 2000.

00–11. Stefan Boschert, Alfred Schmidt, Kunibert G. Siebert, Eberhard Bänsch, Klaus-Werner Benz, Gerhard Dziuk, Thomas Kaiser:
Simulation of Industrial Crystal Growth by the Vertical Bridgman Method, Mai 2000.

00–12. Volker Lehmann, Gerd Teschke:
Wavelet Based Methods for Improved Wind Profiler Signal Processing, Mai 2000.

00–13. Stephan Dahlke, Peter Maass:
A Note on Interpolating Scaling Functions, August 2000.

00–14. Ronny Ramlau, Rolf Clackdoyle, Frédéric Noo, Girish Bal:
Accurate Attenuation Correction in SPECT Imaging using Optimization of Bilinear Functions and Assuming an Unknown Spatially-Varying Attenuation Distribution, September 2000.

00–15. Peter Kunkel, Ronald Stöver:
Symmetric collocation methods for linear differential-algebraic boundary value problems, September 2000.

00–16. Fabian Wirth:
The generalized spectral radius and extremal norms, Oktober 2000.

00–17. Frank Stenger, Ahmad Reza Naghsh-Nilchi, Jenny Niebsch, Ronny Ramlau:
A unified approach to the approximate solution of PDE, November 2000.

00–18. Peter Benner, Enrique S. Quintana-Ortí, Gregorio Quintana-Ortí:
Parallel algorithms for model reduction of discrete–time systems, Dezember 2000.

00–19. Ronny Ramlau:
A steepest descent algorithm for the global minimization of Tikhonov–Phillips functional, Dezember 2000.

01–01. Efficient methods in hyperthermia treatment planning:
Torsten Köhler, Peter Maass, Peter Wust, Martin Seebass, Januar 2001.

01–02. Parallel Algorithms for LQ Optimal Control of Discrete-Time Periodic Linear Systems:
Peter Benner, Ralph Byers, Rafael Mayo, Enrique S. Quintana-Ortí, Vicente Hernández, Februar 2001.

01–03. Peter Benner, Enrique S. Quintana-Ortí, Gregorio Quintana-Ortí:
Efficient Numerical Algorithms for Balanced Stochastic Truncation, März 2001.

01–04. Peter Benner, Maribel Castillo, Enrique S. Quintana-Ortí:
Partial Stabilization of Large-Scale Discrete-Time Linear Control Systems, März 2001.

01–05. Stephan Dahlke:
Besov Regularity for Edge Singularities in Polyhedral Domains, Mai 2001.

01–06. Fabian Wirth:
A linearization principle for robustness with respect to time-varying perturbations, Mai 2001.

01–07. Stephan Dahlke, Wolfgang Dahmen, Karsten Urban:
Adaptive Wavelet Methods for Saddle Point Problems - Optimal Convergence Rates, Juli 2001.

01–08. Ronny Ramlau:
Morozov's Discrepancy Principle for Tikhonov regularization of nonlinear operators, Juli 2001.

01–09. Michael Wolff:
Einführung des Drucks für die instationären Stokes–Gleichungen mittels der Methode von Kaplan, Juli 2001.

01–10. Stephan Dahlke, Peter Maaß, Gerd Teschke:
Reconstruction of Reflectivity Desities by Wavelet Transforms, August 2001.

01–11. Stephan Dahlke:
Besov Regularity for the Neumann Problem, August 2001.

01–12. Bernard Haasdonk, Mario Ohlberger, Martin Rumpf, Alfred Schmidt, Kunibert G. Siebert:
h–p–Multiresolution Visualization of Adaptive Finite Element Simulations, Oktober 2001.

01–13. Stephan Dahlke, Gabriele Steidl, Gerd Teschke:
Coorbit Spaces and Banach Frames on Homogeneous Spaces with Applications to Analyzing Functions on Spheres, August 2001.

02–01. Michael Wolff, Michael Böhm:
Zur Modellierung der Thermoelasto-Plastizität mit Phasenumwandlungen bei Stählen sowie der Umwandlungsplastizität, Februar 2002.

02–02. Stephan Dahlke, Peter Maaß:
An Outline of Adaptive Wavelet Galerkin Methods for Tikhonov Regularization of Inverse Parabolic Problems, April 2002.

02–03. Alfred Schmidt:
A Multi-Mesh Finite Element Method for Phase Field Simulations, April 2002.

02–04. Sergey N. Dachkovski, Michael Böhm:
A Note on Finite Thermoplasticity with Phase Changes, Juli 2002.

02–05. Michael Wolff, Michael Böhm:
Phasenumwandlungen und Umwandlungsplastizität bei Stählen im Konzept der Thermoelasto-Plastizität, Juli 2002.

02–06. Gerd Teschke:
Construction of Generalized Uncertainty Principles and Wavelets in Anisotropic Sobolev Spaces, August 2002.

02–07. Ronny Ramlau:
TIGRA – an iterative algorithm for regularizing nonlinear ill–posed problems, August 2002.

02–08. Michael Lukaschewitsch, Peter Maaß, Michael Pidcock:
Tikhonov regularization for Electrical Impedance Tomography on unbounded domains, Oktober 2002.

02–09. Volker Dicken, Peter Maaß, Ingo Menz, Jenny Niebsch, Ronny Ramlau:
Inverse Unwuchtidentifikation an Flugtriebwerken mit Quetschöldämpfern, Oktober 2002.

02–10. Torsten Köhler, Peter Maaß, Jan Kalden:
Time-series forecasting for total volume data and charge back data, November 2002.

02–11. Angelika Bunse-Gerstner:
A Short Introduction to Iterative Methods for Large Linear Systems, November 2002.

02–12. Peter Kunkel, Volker Mehrmann, Ronald Stöver:
Symmetric Collocation for Unstructured Nonlinear Differential-Algebraic Equations of Arbitrary Index, November 2002.

02–13. Michael Wolff:
Ringvorlesung: Distortion Engineering 2
Kontinuumsmechanische Modellierung des Materialverhaltens von Stahl unter Berücksichtigung von Phasenumwandlungen, Dezember 2002.

02–14. Michael Böhm, Martin Hunkel, Alfred Schmidt, Michael Wolff:
Evaluation of various phase-transition models for 100Cr6 for application in commercial FEM programs, Dezember 2002.

03–01. Michael Wolff, Michael Böhm, Serguei Dachkovski:
Volumenanteile versus Massenanteile - der Dilatometerversuch aus der Sicht der Kontinuumsmechanik, Januar 2003.

03–02. Daniel Kessler, Ricardo H. Nochetto, Alfred Schmidt:
A posteriori error control for the Allen-Cahn Problem: circumventing Gronwall's inequality, März 2003.

03–03. Michael Böhm, Jörg Kropp, Adrian Muntean:
On a Prediction Model for Concrete Carbonation based on Moving Interfaces - Interface concentrated Reactions, April 2003.

03–04. Michael Böhm, Jörg Kropp, Adrian Muntean:
A Two-Reaction-Zones Moving-Interface Model for Predicting $Ca(OH)_2$ Carbonation in Concrete, April 2003.

03–05. Vladimir L. Kharitonov, Diederich Hinrichsen:
Exponential estimates for time delay systems, May 2003.

03–06. Michael Wolff, Michael Böhm, Serguei Dachkovski, Günther Löwisch:
Zur makroskopischen Modellierung von spannungsabhängigem Umwandlungsverhalten und Umwandlungsplastizität bei Stählen und ihrer experimentellen Untersuchung in einfachen Versuchen, Juli 2003.

03–07. Serguei Dachkovski, Michael Böhm, Alfred Schmidt, Michael Wolff:
Comparison of several kinetic equations for pearlite transformation in 100Cr6 steel,
Juli 2003.

03–08. Volker Dicken, Peter Maass, Ingo Menz, Jenny Niebsch, Ronny Ramlau:
Nonlinear Inverse Unbalance Reconstruction in Rotor dynamics,
Juli 2003.